

## Evidence of Feedback Effects in Low-luminosity Active Galactic Nuclei Revealed by JWST Spectroscopy

LULU ZHANG ,<sup>1</sup> CHRIS PACKHAM ,<sup>1,2</sup> ERIN K. S. HICKS ,<sup>3,1,4</sup> RIC I. DAVIES ,<sup>5</sup> DANIEL E. DELANEY ,<sup>4,3</sup> FRANCOISE COMBES ,<sup>6</sup> MIGUEL PEREIRA-SANTAELLA ,<sup>7</sup> ALMUDENA ALONSO-HERRERO ,<sup>8</sup> CLAUDIO RICCI ,<sup>9,10</sup> OMARIA GONZÁLEZ-MARTÍN ,<sup>11</sup> LAURA HERMOSA MUÑOZ ,<sup>8</sup> ISMAEL GARCÍA-BERNETE ,<sup>8</sup> CRISTINA RAMOS ALMEIDA ,<sup>12,13</sup> DIMITRA RIGOPOULOU ,<sup>14,15</sup> FERGUS R. DONNAN ,<sup>16</sup> ENRICA BELLOCCHI ,<sup>17,18</sup> NANCY A. LEVENSON ,<sup>19</sup> MARTIN J. WARD ,<sup>20</sup> SANTIAGO GARCÍA-BURILLO ,<sup>21</sup> AND SEBASTIAN F. HOENIG ,<sup>22</sup>

<sup>1</sup>The University of Texas at San Antonio, One UTSA Circle, San Antonio, TX 78249, USA; [lulu.zhang@utsa.edu](mailto:lulu.zhang@utsa.edu); [l.l.zhangastro@gmail.com](mailto:l.l.zhangastro@gmail.com)

<sup>2</sup>National Astronomical Observatory of Japan, National Institutes of Natural Sciences (NINS), 2-21-1 Osawa, Mitaka, Tokyo 181-8588, Japan

<sup>3</sup>Department of Physics and Astronomy, University of Alaska Anchorage, Anchorage, AK 99508-4664, USA

<sup>4</sup>Department of Physics, University of Alaska, Fairbanks, Alaska 99775-5920, USA

<sup>5</sup>Max-Planck-Institut für extraterrestrische Physik, Postfach 1312, D-85741, Garching, Germany

<sup>6</sup>LUX, Observatoire de Paris, Collège de France, PSL University, CNRS, Sorbonne University, Paris

<sup>7</sup>Instituto de Física Fundamental, CSIC, Calle Serrano 123, 28006 Madrid, Spain

<sup>8</sup>Centro de Astrobiología (CAB), CSIC-INTA, Camino Bajo del Castillo s/n, E-28692 Villanueva de la Cañada, Madrid, Spain

<sup>9</sup>Department of Astronomy, University of Geneva, ch. d'Ecogia 16, 1290, Versoix, Switzerland

<sup>10</sup>Instituto de Estudios Astrofísicos, Facultad de Ingeniería y Ciencias, Universidad Diego Portales, Av. Ejército Libertador 441, Santiago, Chile

<sup>11</sup>Instituto de Radioastronomía and Astrofísica (IRyA-UNAM), 3-72 (Xangari), 8701, Morelia, Mexico

<sup>12</sup>Instituto de Astrofísica de Canarias, Calle Vía Láctea, s/n, E-38205, La Laguna, Tenerife, Spain

<sup>13</sup>Departamento de Astrofísica, Universidad de La Laguna, E-38206, La Laguna, Tenerife, Spain

<sup>14</sup>Department of Physics, University of Oxford, Keble Road, Oxford OX1 3RH, UK

<sup>15</sup>School of Sciences, European University Cyprus, Diogenes street, Engomi, 1516 Nicosia, Cyprus

<sup>16</sup>Department of Astronomy and Astrophysics, University of California, San Diego, La Jolla, CA 92093, USA

<sup>17</sup>Departamento de Física de la Tierra y Astrofísica, Fac. de CC. Físicas, Universidad Complutense de Madrid, 28040 Madrid, Spain

<sup>18</sup>Instituto de Física de Partículas y del Cosmos IPARCOS, Fac. CC. Físicas, Universidad Complutense de Madrid, 28040 Madrid, Spain

<sup>19</sup>Space Telescope Science Institute, 3700 San Martin Drive Baltimore, Maryland 21218, USA

<sup>20</sup>Centre for Extragalactic Astronomy, Durham University, South Road, Durham DH1 3LE, UK

<sup>21</sup>Observatorio Astronómico Nacional (OAN-IGN)-Observatorio de Madrid, Alfonso XII, 3, 28014, Madrid, Spain

<sup>22</sup>School of Physics and Astronomy, University of Southampton, Southampton SO17 1BJ, UK

## ABSTRACT

This letter presents an analysis of the infrared ( $\sim 3 - 28 \mu\text{m}$ ) spectra extracted from the nuclear ( $r < 150 \text{ pc}$ ) regions of four low-luminosity active galactic nuclei (AGN), observed by JWST NIRSpec/IFU and MIRI/MRS as an extension of the Galaxy Activity, Torus, and Outflow Survey (GATOS). We find that, compared to higher-luminosity AGN, these low-luminosity AGN exhibit distinct properties in their emission of ionized gas, polycyclic aromatic hydrocarbons (PAHs), and molecular hydrogen ( $\text{H}_2$ ). Specifically, the low-luminosity AGN exhibit relatively weak high-ionization potential lines (e.g., [Ne V] and [O IV]), and the line ratios suggest that fast radiative shocks (with  $v_s$  of  $\sim 100 \text{ km s}^{-1}$ ) are the primary excitation source of ionized gas therein. Under the low-excitation conditions of their nuclear regions, these low-luminosity AGN generally exhibit a higher fraction of PAHs with large size ( $N_C \gtrsim 200$ ), reflecting the preferential destruction of smaller PAH molecules by AGN feedback. Furthermore, the  $\text{H}_2$  transitions in these low-luminosity AGN are not fully thermalized, with slow, plausibly jet-driven molecular shocks (with  $v_s \leq 10 \text{ km s}^{-1}$ ) likely being the extra excitation source. Taken together with results from the literature, these findings indicate that feedback operates in both low- and high-luminosity AGN, albeit its impact varies with AGN luminosity. In particular, systematic variations in PAH band ratios are found across AGN, demonstrating the differing influence of feedback in AGN of varying luminosities and highlighting the potential of PAH band ratios as diagnostics for distinguishing kinetic- and radiative-mode AGN feedback.

**Keywords:** galaxies: active galactic nucleus — galaxies: ISM — infrared: ISM — galaxies: star formation

## 1. INTRODUCTION

Widely regarded to coevolve with their host galaxies (e.g., Magorrian et al. 1998; Ferrarese & Merritt 2000; Gebhardt et

al. 2000; and see review Kormendy & Ho 2013), supermassive black holes (SMBHs) reside in most, if not all, massive galaxies and can influence their hosts and large-scale surroundings in a variety of ways (e.g., Schaye et al. 2015; Pillepich et al. 2018; Davé et al. 2019; and see reviews Fabian 2012; Heckman & Best 2014; Harrison & Ramos Almeida 2024). In the local universe, the most prevalent accreting SMBHs are low-luminosity active galactic nuclei (AGN), often manifesting as low-ionization nuclear emission-line regions (LINERs; Heckman 1980) characterized by very low radiative efficiency, faint luminosities, and more pronounced jet-like features (e.g., Ho et al. 1993, 2003; Ho 1999, 2009; Di Matteo et al. 2003; Pellegrini et al. 2003; Mason et al. 2012; Fernández-Ontiveros et al. 2023; and see review Ho 2008). In contrast to vigorously accreting, high-luminosity AGN that can expel gas from their host galaxies through *the radiative (or quasar) mode* feedback (e.g., winds/outflows; Di Matteo et al. 2005; Hopkins et al. 2008a; Harrison et al. 2014), these highly sub-Eddington, low-luminosity AGN can in theory redirect most of their accretion power from radiation to kinetic energy (see reviews McNamara & Nulsen 2007; Yuan & Narayan 2014), and interact with their surroundings mainly via *the kinetic (or radio/jet) mode* feedback (e.g., jets/shocks; Weinberger et al. 2017; Davé et al. 2019).

The kinetic mode feedback has attracted considerable attention given its crucial role in sustaining the quenching phase of massive bulges and elliptical galaxies (see reviews Fabian 2012; Heckman & Best 2014). These systems are theoretically regarded as the ultimate fate of galaxy evolution and are of great importance for our understanding of AGN–host co-evolution (Hopkins et al. 2006, 2008a,b). Given their significance in the evolutionary pathway of galaxies, the kinetic mode feedback has been widely studied through numerical simulations and optical/X-ray/radio observations (e.g., Di Matteo et al. 2003; Nesvadba et al. 2017; Pillepich et al. 2018; Davé et al. 2020; Fernández-Ontiveros et al. 2023; Wang et al. 2024; Ilha et al. 2025). JWST (Gardner et al. 2023), with its superb sensitivity and broad wavelength coverage, offers new opportunities to probe the specific effects of kinetic-mode AGN feedback through the rich information on gas content, kinematics, and excitation provided by abundant infrared diagnostics relatively immune from dust extinction, including a broad suite of ionized emission lines, H<sub>2</sub> transitions, and PAH features (e.g., Pereira-Santaella et al. 2022; García-Bernete et al. 2022a, 2024; Donnan et al. 2023; Hernandez et al. 2023; Zhang & Ho 2023; Chown et al. 2024; Goold et al. 2024; Hermosa Muñoz et al. 2025a,b; Peeters et al. 2024; Zhang et al. 2024a,b; Alonso Herrero et al. 2025; Ceci et al. 2025; López et al. 2025; Ogle et al. 2025; Ramos Almeida et al. 2025).

Combined with theoretical calculations (e.g., Kristensen et al. 2023; Rigopoulou et al. 2024; López et al. 2025; Zhang et

al. 2025), infrared emission features of ionized gas, H<sub>2</sub>, and PAHs together can provide strong constraints on the physical conditions around AGN and hence underlying feedback mechanisms. In particular, the intrinsic and relative intensities of individual PAH features at different wavelengths (e.g., 3.3, 6.2, 7.7, 8.6, 11.3, 12.7, and 17.0  $\mu\text{m}$ ) vary markedly across different galactic environments (e.g., Genzel et al. 1998; Peeters et al. 2002; Kaneda et al. 2005; Farrah et al. 2007; Gordon et al. 2008; Hunt et al. 2010; Lebouteiller et al. 2011), and the variation is particularly pronounced in the hostile environments around AGN (e.g., Smith et al. 2007; O'Dowd et al. 2009; Diamond-Stanic & Rieke 2010; Sales et al. 2010; García-Bernete et al. 2022a,b, 2024; Zhang et al. 2022, 2024b; Lai et al. 2023; Zhang & Ho 2023; Donnelly et al. 2024). Specifically, low-luminosity AGN, especially LINERs, exhibit on kilo-parsec (kpc) scales relatively lower PAH 6.2  $\mu\text{m}$ /7.7  $\mu\text{m}$  and higher 11.3  $\mu\text{m}$ /7.7  $\mu\text{m}$  ratios compared to star-forming galaxies (SFGs), which can be attributed to the preferential destruction of the smaller PAHs by shocks within the overall PAH population (Zhang et al. 2022). In addition, low-redshift quasars, where the radiative mode feedback is likely to dominate, exhibit even lower PAH 6.2  $\mu\text{m}$ /7.7  $\mu\text{m}$  but also lower 11.3  $\mu\text{m}$ /7.7  $\mu\text{m}$  ratios (Xie & Ho 2022). The distinct PAH characteristics observed in low- and high-luminosity AGN provide preliminary evidence that PAH features may serve as useful diagnostics for distinguishing between different feedback modes.

This letter is the first in a series designed to investigate the kinetic mode feedback in a sample of four low-luminosity AGN, through analysis of infrared emission features obtained from dedicated and archival JWST spectroscopic observations. Low-luminosity AGN are targeted here because kinetic-mode feedback is expected to be prevalent in these systems as outlined above, although growing evidence indicates that such feedback can also be important in high-luminosity AGN (e.g., Ilha et al. 2025; Roy et al. 2025; Vayner et al. 2025). This first paper focuses on the analysis of the infrared ( $\sim 3 - 28 \mu\text{m}$ ) spectra extracted from the nuclear ( $r < 150 \text{ pc}$ ) regions of the sample, while the spatially resolved analysis over a larger field of view (FoV) will be presented in subsequent papers. After introducing the targets and observations, as well as the data reduction, spectral extraction, and decomposition in Section 2, we present the main results on the distinct emission properties of ionized gas, PAHs, and H<sub>2</sub> in the nuclear regions of the four low-luminosity AGN in Section 3. We further discuss the underlying mechanisms responsible for the systematically distributed PAH band ratios observed across diverse galactic systems in Section 4. A summary of the main points of this letter is presented in Section 5.

## 2. OBSERVATION AND ANALYSIS

### 2.1. Targets and Observations

The sample analyzed here consists of four low-luminosity AGN selected by JWST Cycle 3 General Observer (GO) Program 4972 (PI: L. Zhang) from the Spitzer Infrared Nearby Galaxies Survey (SINGS; [Kennicutt et al. 2003](#)). The SINGS survey is a comprehensive infrared imaging and (mapping-mode) spectroscopic survey by the Spitzer with a rich repository of ancillary multi-band data sets (see e.g., [Dale et al. 2006](#); [Smith et al. 2007](#); [Moustakas et al. 2010](#)). GO Program 4972 is among the first JWST programs dedicated to low-luminosity AGN, and it is the first designed explicitly to assess the effectiveness of PAH features as diagnostics of the kinetic mode feedback. To this end, we proposed to investigate the spatially resolved characteristics of PAH features and other infrared emission lines in the  $\sim 3 - 28 \mu\text{m}$

wavelength range around these low-luminosity AGN. Specifically, this sample includes all SINGS AGN that are classified as LINERs in the optical band ([Smith et al. 2007](#)) and also exhibit prominent PAH features in their Spitzer/IRS spectra extracted from the central  $10''$  regions ([Zhang et al. 2022](#)). Additionally, all four LINERs show evidence of mechanical processes (radio cores and/or shocked gas) associated with their nuclei (e.g., [Nagar et al. 2002, 2005](#); [Nemmen et al. 2006, 2014](#); [Nyland et al. 2013](#); [Pellegrini et al. 2013](#); [Mezcua & Prieto 2014](#)). Note that JWST spectroscopy of NGC 4736 were already included in JWST Cycle 1 GO Program 2016 (PI: A. Seth; [Goold et al. 2024](#)), GO Program 4972 therefore only requested JWST spectroscopy for NGC 1097, NGC 1266, and NGC 3190. See Table 1 for basic properties of the sample.

**Table 1.** Basic Properties of the Sampled Low-luminosity AGN

Target	Hubble Type	$z$	$D$	$i$	$\log L_{(2-10)\text{keV}}^{\text{Xray}}$	$\log L_{1.4\text{GHz}}^{\text{radio}}$	$\log M_{\text{BH}}$	$\log \lambda_{\text{Edd}}$
(1)	(2)	(3)	(4)	(5)	(6)	(7)	(8)	(9)
NGC 1097 <sup>†</sup>	SBB	0.004240	17.2	35	40.8	22.2	8.1	-4.2
NGC 1266 <sup>‡</sup>	SB0	0.007238	29.4	50	40.6	22.0	6.2	-2.5
NGC 3190	Sa	0.004370	24.5	83	39.6	21.5	8.2	-5.5
NGC 4736	Sab	0.001027	5.1	35	38.6	20.9	7.2	-5.5

NOTE—Column (1): Target names; Column (2-5): Hubble types, redshifts, redshift-independent distances, and disk inclinations taken from the NASA/IPAC Extragalactic Database (NED); Column (6): Nuclear 2–10 keV X-ray luminosities taken from [Ho \(2009\)](#) unless otherwise specified (the values in this table have been adjusted according to the adopted distances); Column (7): Nuclear 1.4 GHz radio luminosity densities derived from VLA flux densities retrieved from the NED. Column (8): Black hole masses derived from the  $M_{\text{BH}} - \sigma_*$  relation of [Greene et al. \(2020\)](#) unless otherwise specified, with  $\sigma_*$  from [Ho et al. \(2009\)](#). Column (9): Eddington ratios  $\lambda_{\text{Edd}} = L_{\text{bol}}/L_{\text{Edd}}$ , with  $L_{\text{bol}} = 15.8 \times L_{(2-10)\text{keV}}^{\text{Xray}}$  and  $L_{\text{Edd}} = 1.26 \times 10^{38} (M_{\text{BH}}/\text{M}_\odot)$ . <sup>[†]</sup>  $L_{(2-10)\text{keV}}^{\text{Xray}}$  and  $M_{\text{BH}}$  are taken from [Cisternas et al. \(2013\)](#). <sup>[‡]</sup>  $L_{(2-10)\text{keV}}^{\text{Xray}}$  and  $M_{\text{BH}}$  are taken from [Chen et al. \(2023\)](#) and [Alatalo et al. \(2015\)](#), respectively.

NGC 1097, NGC 1266, and NGC 3190 were observed under GO Program 4972 between November 2024 and May 2025 with JWST NIRSpec/IFU ([Böker et al. 2022](#); [Jakobsen et al. 2022](#)) using the G395H/F290LP grating/filter combination and with MIRI/MRS ([Wells et al. 2015](#); [Wright et al. 2023](#)) covering all four channels. JWST spectroscopic observations of NGC 4736 (including the above instrumental combinations) were carried out in June 2024. The two programs both adopted a 4-point dither pattern for NIRSpec/IFU and MIRI/MRS exposures of the targets, focusing on their most central  $\sim 300 - 600$  pc regions, where AGN activity dominates ([Moustakas et al. 2010](#)). The total on source exposure times range from 584 – 875s and 777 – 999s for NIRSpec/IFU and MIRI/MRS observations using NR-SIRS2RAPID and FASTR1 readout patterns, respectively. In addition, GO Program 4972 adopted a recommended 2-

point dither pattern while GO Program 2016 used a 1-point non-dither pattern for the corresponding MIRI/MRS background observations. Both programs also adopted a 1-point non-dither pattern for the NIRSpec/IFU leakage corrections. More details about the observational configurations are included in the program information webpages of programs [GO 4972](#) and [GO 2016](#). The observations of the four targets can be accessed via doi: [10.17909/psw5-s410](https://doi.org/10.17909/psw5-s410).

### 2.2. Data Processing and Nuclear Spectrum Extraction

The data were reduced using the JWST Science Calibration Pipeline (v1.18.0; [Bushouse et al. 2025](#)) with the context 1364 for the Calibration References Data System. Particularly, residual fringes remain with the standard fringe removal, which could have an influence on weak spectral features ([Argyriou et al. 2020](#); [Gasman et al. 2023](#)).

Therefore, the `residual_fringe` correction, disabled by default in the standard JWST pipeline, was activated to correct the fringe residuals (Law et al. 2023). In addition, the `imprint_subtract` function was activated in JWST NIRSpec/IFU pipeline for leakage correction and the default `master_bg` function was adopted in JWST MIRI/MRS pipeline for background subtraction. The JWST NIRSpec/IFU and MIRI/MRS pipelines ultimately produced one and twelve spectral data cubes for each target, respectively. The NIRSpec/IFU spectral data cube of each target has a FoV of  $\sim 3''.4 \times 3''.4$ , spanning the  $2.87 - 5.27 \mu\text{m}$  wavelength range with the spectral resolution of  $\sim 2000 - 4000$  (Jakobsen et al. 2022; Shajib et al. 2025). The twelve MIRI/MRS spectral data cubes of each target have FoVs ranging from  $\sim 3''.6 \times 4''.5$  (ch1) to  $\sim 7''.0 \times 8''.5$  (ch4) depending on the channel, together spanning the  $4.90 - 27.90 \mu\text{m}$  wavelength range with the spectral resolution of  $\sim 4000 - 2000$  (Argyriou et al. 2023; Pontoppidan et al. 2024).

To extract spectra from the nuclear regions of the targets, we first characterized the unresolved AGN emission and estimated its wavelength-dependent contribution to the total flux within the central aperture. To this end, we fitted each slice in the data cubes with a model consisting of two two-dimensional Gaussian functions, one circular for the unresolved AGN component and the other allowed to be elliptical for the host galaxy, plus a uniform background. In this way, we obtained wavelength-dependent full widths at half maximum (FWHMs) for the AGN component that are consistent with those measured from JWST/MIRI MRS observations of point-like stars by Zhang & Ho (2023). More importantly, the unresolved AGN emission in all NIRSpec/IFU and MIRI/MRS bands were found to account for over 95% of the total flux within radii equal to their FWHMs at all wavelengths for these targets. We then extracted the nuclear spectra using wavelength-dependent apertures from the full set of spectral data cubes for each target. The aperture center in each sub-band is the median position of the fitted AGN component within that sub-band, and the aperture radius is given by  $r = 0.033 \times \lambda + 0.106$  (e.g.,  $r = 0''.436$  at  $\lambda = 10 \mu\text{m}$ , corresponding to  $r \lesssim 60 \text{ pc}$  at the distances of the four targets). The adopted aperture radius approximately equals to the FWHM value of the fitted point-spread-function-like (PSF-like) AGN component at each wavelength.

Subsequently, we applied the same wavelength-dependent aperture correction strategy to the extracted MIRI/MRS spectra as adopted by González-Martín et al. (2025), with the pre-computed aperture correction factors ( $\sim 1.37 - 1.47$ ) based on in-flight observational MIRI/MRS PSFs.<sup>1</sup> Since

no such calibration file exists for NIRSpec/IFU observations, we derived the aperture correction factors ( $\sim 1.30 - 1.32$ ) from the encircled energy curves of theoretical NIRSpec/IFU PSFs computed by Python package STPSF, and applied them for the extracted NIRSpec/IFU spectra. Finally, all aperture-corrected sub-band nuclear spectra were stitched together to produce a complete infrared spectrum spanning the  $\sim 3 - 28 \mu\text{m}$  wavelength range for each target. Therein, systematic discontinuities, plausibly arising from data reduction uncertainties including aperture correction, between NIRSpec/IFU and MIRI/MRS sub-bands ( $\lesssim 10\%$ ) and within some NIRSpec/IFU sub-bands ( $\lesssim 5\%$ ) were corrected using constant scaling factors determined from the median fluxes in the overlapping or adjacent wavelength ranges.

### 2.3. Spectral Decomposition and Measurement

As illustrated in Figure 1, we first decomposed the PAH features from the extracted spectra through multi-component fitting, after masking all emission lines as well as the two adjacent CO<sub>2</sub> and CO features (of strong detection only in NGC 1266). The multi-component model consists of a series of Drude profiles for individual PAH features, multiple modified blackbodies for dust components, and a black body of 5000 K mimic the stellar continuum. Specifically, the Drude profiles with fixed widths are primarily adopted from Draine & Li (2007) with some updates according to Lai et al. (2020), Donnan et al. (2023), and Draine et al. (2025). The fixed temperatures of the modified blackbodies range from 35 to 1200 K, in accordance with previous studies (i.e., Smith et al. 2007; Donnan et al. 2023; Zhang et al. 2024b). Moreover, all the model components are subject to foreground extinction, adopting the infrared extinction curve of Smith et al. (2007) (primarily for the silicate absorption features at 9.7 and  $18 \mu\text{m}$ ), plus additional ice absorption features as reviewed by Boogert et al. (2015) (see Table A1 in Appendix C for details of the adopted ice absorption features for each target). The decomposition was performed using the Bayesian Markov Chain Monte Carlo sampler `emcee` in the Python environment, with the median and standard deviation of the posterior distribution of each parameter adopted as the final estimate and its corresponding uncertainty (see Table A2 in the Appendix C for the PAH flux measurements).

We then fitted all ionized emission lines, as well as the H<sub>2</sub> pure rotational (H<sub>2</sub>  $S(J)$ , e.g., H<sub>2</sub>  $S(3)$ ) and ro-vibrational (H<sub>2</sub>  $\nu_{\text{up}}-\nu_{\text{low}} O(J)$ , e.g., H<sub>2</sub> 1-0  $O(5)$ )<sup>2</sup> transitions, individually with single- and double-Gaussian profiles plus a local linear continuum, using the Levenberg-Marquardt least-squares minimization algorithm. From visual inspection of the fits, we found that a double-Gaussian profile was required

<sup>1</sup> Detailed information is included in the CRDS calibration file `jwst_miri_apcorr_0008.asdf`, and the wavelength-dependent aperture radius  $r = 0.033 \times \lambda + 0.106$  is also derived from this file.

<sup>2</sup> Only a few of the  $O$ -branch ro-vibrational transitions fall within the wavelength range covered by the nuclear spectra analyzed in this study.

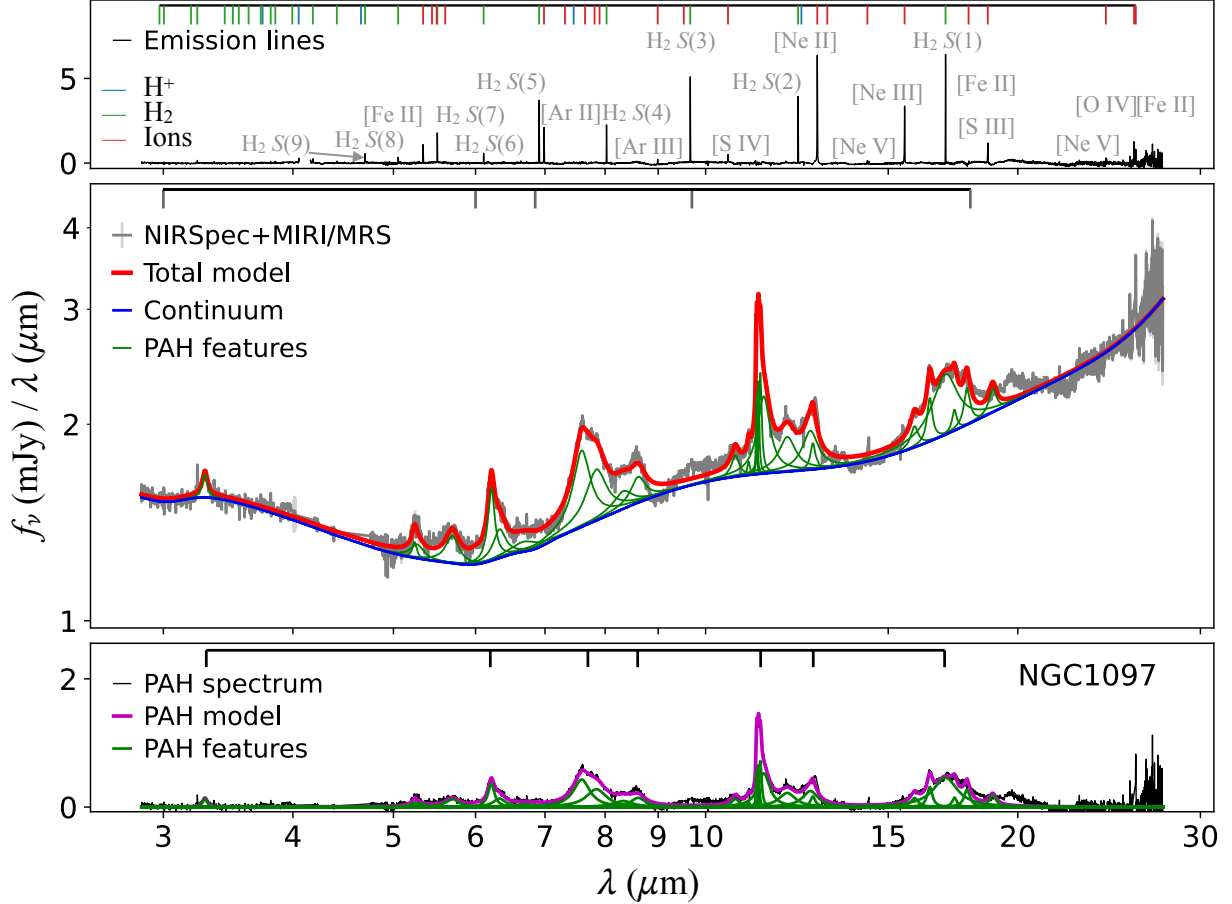


**Figure 1.** Top panel: The residual emission line spectrum obtained by subtracting the best-fit model (red curve in the middle panel) from the nuclear  $\sim 3 - 28 \mu\text{m}$  spectrum. The positions of key emission lines (not necessarily all detected) are indicated by short-colored lines at the top. Middle panel: Illustrations of the multi-component fitting for PAH feature decomposition (see details in Section 2.3), with the positions of the two silicate absorption features and the adopted ice absorption features for each target indicated by short-gray lines at the top. The gray curve is the nuclear NIRSpec/IFU + MIRI/MRS spectra, after masking the emission lines, as well as the CO<sub>2</sub> and CO features marked in panel b. The red curve shows the best-fit model, the blue curve shows the sum of all continuum components (i.e., stellar and dust continuum), and these green curves are Drude profiles representing individual PAH features. Bottom panel: The residual PAH spectrum (black curve) obtained by subtracting all continuum components from the masked nuclear NIRSpec/IFU + MIRI/MRS spectrum. The positions of prominent PAH features around 3.3, 6.2, 7.7, 8.6, 11.3, 12.7, and 17.0  $\mu\text{m}$  are indicated by short-black lines at the top. Same as in the middle panel, these green curves are Drude profiles representing individual PAH features, and the magenta curve shows the sum of all green curves, i.e., the modeled PAH spectrum. All x-axes and the y-axis of the middle panel are in logarithmic scale, while the other y-axes are in linear scale, and all spectra are in the rest frame. See Figures A1, A2, and A3 in Appendix A for the same plots for NGC 1266, NGC 3190, and NGC 4736.

for all ionized emission lines, whereas a single-Gaussian profile was sufficient for the H<sub>2</sub> transitions. To obtain more robust statistics, each emission line spectrum was perturbed with random noise at the level of its uncertainty, and the fitting was repeated 100 times. The median and standard deviation of the 100 fits were adopted as the final flux estimate and its corresponding uncertainty for each emission line, respectively. Additionally, the fluxes of all emission lines were corrected for dust extinction using the extinction values derived from the multi-component full-spectrum fitting described above. See Tables A3 and A4 in Appendix C for the

flux measurements of prominent ionized emission lines, as well as the H<sub>2</sub> pure rotational and ro-vibrational transitions detected in the nuclear spectra.

### 3. RESULTS

In this section, we characterize the emission from ionized gas, PAHs, and H<sub>2</sub> in the nuclear regions of the four low-luminosity AGN. By integrating insights from model results (Guillard et al. 2012; Kristensen et al. 2023; Rigopoulou et al. 2024; Zhang et al. 2025) and comparing with emission line and PAH measurements for nuclear regions and circumnuclear apertures of higher-luminosity Seyferts ( $\log L_{(2-10)\text{keV}}^{\text{Xray}}$

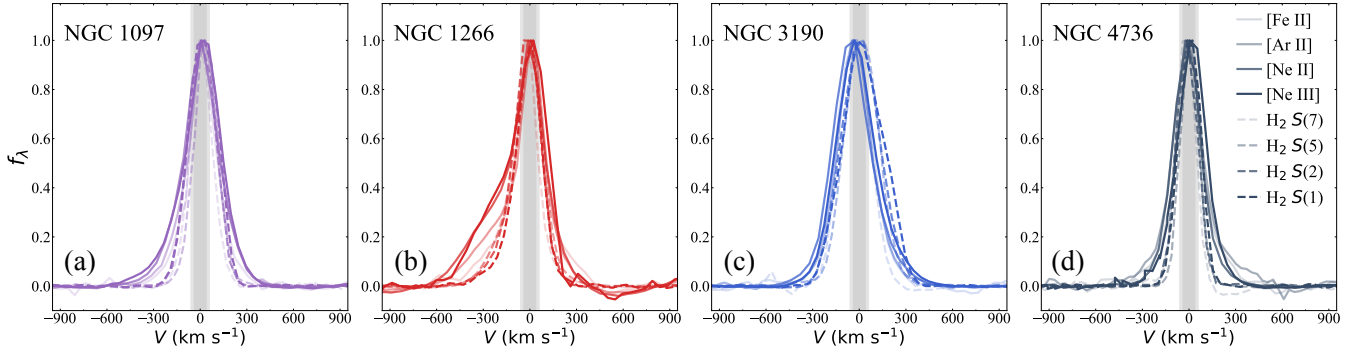


**Figure 2.** Normalized nuclear emission line profiles of [Fe II], [Ar II], [Ne II], and [Ne III], shown in order of increasing ionization potential from lighter to darker colors, along with  $H_2$   $S(7)$ ,  $H_2$   $S(5)$ ,  $H_2$   $S(2)$ , and  $H_2$   $S(1)$ , whose wavelengths are close to those of the ionized emission lines with the same colors, respectively. The gray shaded regions in each panel indicate the range of instrumental broadening (FWHM) at the wavelengths of these lines. All line profiles are shown in the rest frame.

$= 40.9 - 43.1$ ; Zhang et al. 2024a,b), we find that shocks (i.e., the kinetic mode feedback) play a central role in shaping the nuclear environments of these low-luminosity AGN.

### 3.1. Emission Line Profiles and Kinematics

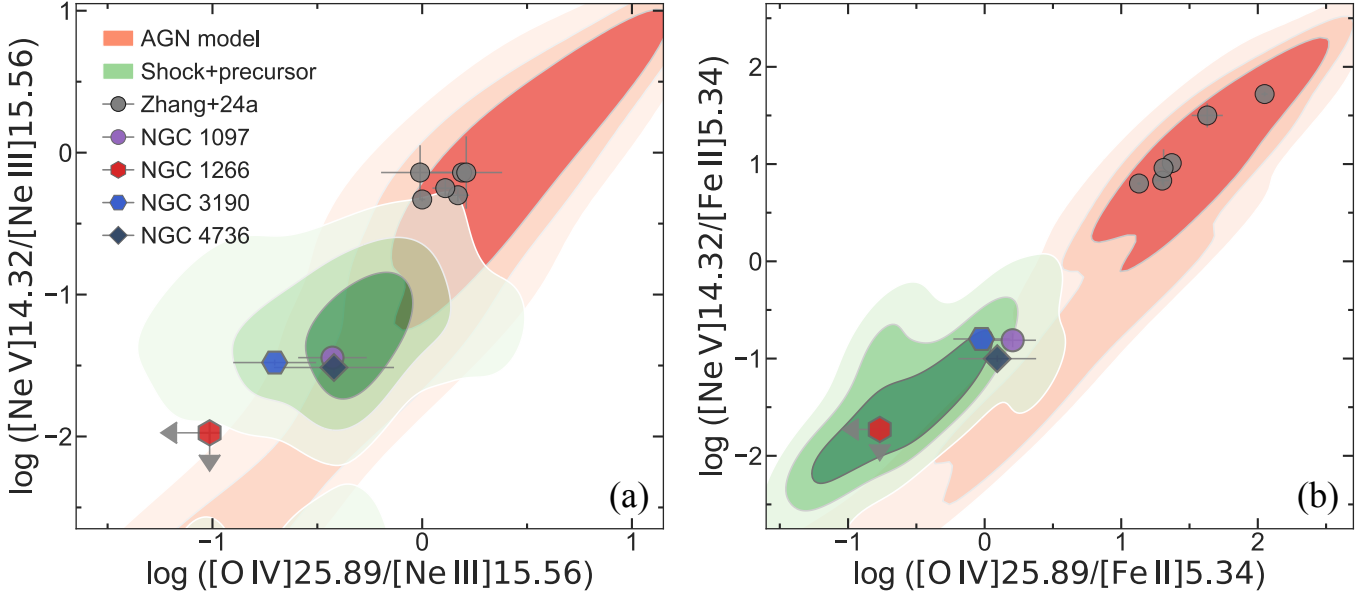
As shown in Figures 1, A1, A2, and A3, the nuclear spectra of the four targets exhibit variations in continuum shape, extinction strength, PAH feature intensity (especially at shorter wavelengths) and in their emission line spectra. For instance, NGC 1266 exhibits the steepest dust-continuum slope (Figure A1), more like the starburst-dominated Spitzer/IRS spectra, whereas the other three targets show v-shape dust continua consistent with the LINER-dominated Spitzer/IRS spectra presented by González-Martín et al. (2015; Figure 5 therein). NGC 1266 also shows the strongest extinction, relatively stronger short-wavelength PAH emission, and weaker high-ionization emission lines, implying the presence of unique evolutionary processes (see also e.g., Davis et al. 2012; Pellegrini et al. 2013; Alatalo et al. 2014; Otter et al. 2024). More detailed discussions of these variations are presented in the following subsections, while this subsection focuses on the kinematics of the ionized and molecular gas components revealed in the nuclear emission line spectra. Although a spatially resolved analysis, to be presented in subsequent papers, will better constrain the kinematic properties of these gas components, the kinematics of the emission lines in the nuclear spectra already provide important insights into the underlying feedback mechanisms.

Figure 2 shows the normalized profiles of four pairs of  $H_2$  and ionized emission lines in the nuclear spectra, with each pair of emission lines having similar wavelengths. The key result in Figure 2 is that all ionized emission lines are generally broader than the paired  $H_2$  lines, primarily due to the bilateral high-velocity components (especially those on the blue-shifted side) in ionized emission lines. Although this trend is less pronounced in NGC 3190 (see Figure 2c), the ionized emission lines in this galaxy are systematically

blue-shifted relative to the  $H_2$  emission lines. Overall, the widths of the ionized emission lines increase with ionization potential, a trend also observed in the nuclear regions of higher-luminosity Seyferts (e.g., Armus et al. 2023; Hermosa Muñoz et al. 2024; Zhang et al. 2024a). The markedly different kinematics of the ionized gas, particularly the highly ionized component, relative to  $H_2$  imply the presence of ionized outflows launched from these nuclear regions, which we will examine in more detail in subsequent papers. The preliminary results in Figure 2 suggest that NGC 1266 exhibits the strongest ionized outflows among the four targets, whereas the weak outflow signature in NGC 3190 may be partly attributable to its almost edge-on orientation. More importantly, these results indicate that the ionized gas in the nuclear regions is, to some extent, decoupled from the molecular gas and appears to be more sensitive to AGN-driven outflows, as also discussed in our recent works (e.g., Pereira-Santaella et al. 2022; Davies et al. 2024; Alonso Herrero et al. 2025; Riffel et al. 2025). This decoupling is important for unifying the different physical conditions around the AGN inferred from the ionized emission lines and  $H_2$  transitions, as detailed in the following.

### 3.2. Ionized Emission Lines and Diagnostics

Ratios of infrared emission lines with different ionization potentials (IPs) and critical densities have been long proposed as powerful diagnostics of galaxy properties (e.g., Spinoglio & Malkan 1992; Genzel et al. 1998; Thornley et al. 2000; Dale et al. 2006; Armus et al. 2007; Pereira-Santaella et al. 2010, 2017; Feltre et al. 2023; Zhang et al. 2025). Figure 3 presents two diagnostic diagrams showing high-to-low ionization potential line ratios, along with the distributions of model results for AGN and fast radiative shocks. The AGN and fast radiative shock (including the shock precursor) models are from Zhang et al. (2025) computed using MAPPINGS V (Sutherland & Dopita 2017). Specifically, the AGN models shown in Figure 3 adopt input parameters in-



**Figure 3.** Diagnostic diagrams of ionized emission line ratios: (a)  $[\text{Ne V}]/[\text{Ne III}]$  versus  $[\text{O IV}]/[\text{Ne III}]$ , and (b)  $[\text{Ne V}]/[\text{Fe II}]$  versus  $[\text{O IV}]/[\text{Fe II}]$ . The reddish and greenish contours show the distributions of model results computed by Zhang et al. (2025) for AGN and fast radiative shocks (including the shock precursor), respectively, with each contour enclosing 30%, 60%, and 90% of the model results from inside to outside. The colored and gray data points represent measurements for the nuclear regions of the four low-luminosity AGN studied here and the six higher-luminosity Seyferts studied by Zhang et al. (2024a), respectively. The line ratios of NGC 1266 are marked as upper limits because  $[\text{Ne V}]$  and  $[\text{O IV}]$  flux measurements of this galaxy are below three times of the standard deviation noise of local continuum.

cluding the ionization parameter  $\log U$ , the AGN spectrum peak energy  $\log (E_{\text{peak}}/\text{keV})$ , the metallicity, and the gas pressure  $\log (P/k)$ , ranging from  $-4.3$  to  $-1.3$ ,  $-2.1$  to  $-0.9$ ,  $0.2$  to  $2 Z_{\odot}$ , and  $5.5$  to  $8.5$ , respectively. The shock models, in comparison, adopt input parameters including the shock velocity  $v_s$ , the pre-shock density  $n_{\text{H}}$ , the magnetic to ram pressure ratio  $\eta_{\text{M}}$ , and the metallicity, ranging from  $100$  to  $500 \text{ km s}^{-1}$ ,  $1$  to  $10^4 \text{ cm}^{-3}$ ,  $0.0$  to  $0.1$ , and  $0.2$  to  $2 Z_{\odot}$ , respectively (see Zhang et al. 2025 for more details).

Figure 3 shows that the ionized gas in the four low-luminosity AGN is less highly excited, exhibiting weaker emission lines of high ionization potential compared to the nuclear  $r = 0''.75$  regions of six higher-luminosity Seyferts (see also Goold et al. 2024; Alonso Herrero et al. 2025; Hermosa Muñoz et al. 2025a). This trend is the most evident for NGC 1266, with the fluxes of  $[\text{Ne V}]14.32\mu\text{m}$  (IP: 97.1 eV) and  $[\text{O IV}]25.89\mu\text{m}$  (IP: 54.9 eV) lines in the nuclear region of this galaxy below three times of the standard deviation noise of local continuum. The extremely weak high ionization potential lines in this post-starburst galaxy NGC 1266 is at least partially due to the highly obscured condition in the nuclear region of this galaxy, as indicated by the strong silicate and ice absorption features (see Figure 1b). The highly obscured condition can be attributed to a gravitational encounter driving molecular gas into the nucleus (Alatalo et al. 2014 and references therein). Upon close inspection of their nuclear spectra around specific wave-

lengths, we find that additional high ionization potential lines such as  $[\text{Mg IV}]4.49\mu\text{m}$  (IP: 80.1 eV),  $[\text{Mg V}]5.61\mu\text{m}$  (IP: 109.2 eV), and  $[\text{Ne VI}]7.65\mu\text{m}$  (IP: 126.2 eV) are also detectable in the nuclear regions of NGC 1097 and NGC 3190, but not in NGC 1266 and NGC 4736, with the latter galaxy having  $\log L_{(2-10)\text{keV}}^{X\text{ray}} < 40$ . Interestingly,  $[\text{Ar V}]$  lines at  $7.90$  and  $13.10 \mu\text{m}$  (IP: 59.6 eV) are absent in the nuclear spectra of the four low-luminosity AGN, whereas  $[\text{Ar VI}]$  line at  $4.53 \mu\text{m}$  (IP: 74.8 eV) is tentatively detected in the nuclear spectra of NGC 1097 and NGC 3190. A comprehensive analysis of these ionized emission lines is deferred to a dedicated paper.

In addition to the generally low-excitation conditions in these low-luminosity AGN, another key result shown by Figure 3 is that the ionized gas in these sources appears to be primarily excited by fast ( $\sim 100\text{s km s}^{-1}$ ) radiative shocks, whereas the higher-luminosity Seyferts are dominated by AGN photoionization. This trend is especially evident in Figure 3(b), which involves  $[\text{Fe II}]5.34\mu\text{m}$  line (IP: 7.9 eV) that is sensitive to shocks (e.g., Forbes & Ward 1993; Mouri et al. 2000; Koo et al. 2016). We note that not only  $[\text{Fe II}]5.34\mu\text{m}$  line, but also  $[\text{Fe II}]17.93\mu\text{m}$  and  $[\text{Fe II}]25.99\mu\text{m}$  lines are of detection in the four low-luminosity AGN, albeit the latter two lines in NGC 1266 are below three times of the standard deviation noise of local continuum. Nevertheless, the ionized gas in the nuclear region of NGC 1266 is plausibly dominated by shock excitation, as further discussed below

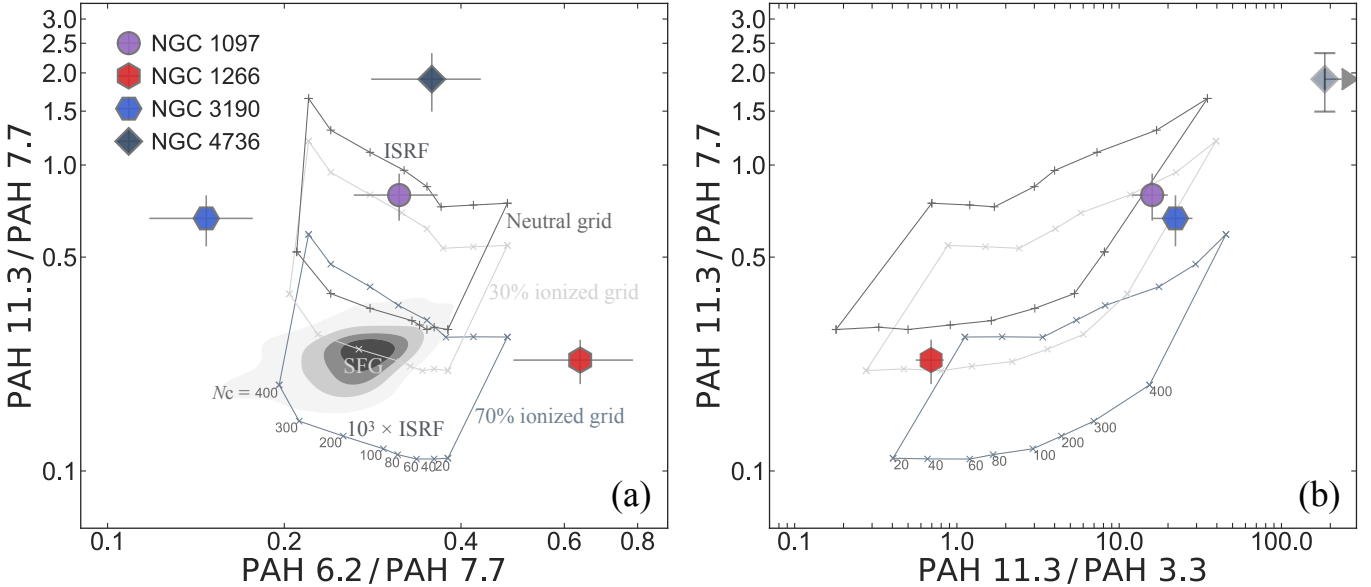


**Figure 4.** Diagnostic diagrams of PAH band ratios: (a)  $11.3 \mu\text{m}/7.7 \mu\text{m}$  versus  $6.2 \mu\text{m}/7.7 \mu\text{m}$  and (b)  $11.3 \mu\text{m}/7.7 \mu\text{m}$  versus  $11.3 \mu\text{m}/3.3 \mu\text{m}$ , with the colored data points representing measurements in the nuclear regions of the four low-luminosity AGN. The gray contours represent the PAH band ratio distribution of spatially resolved regions in SINGS SFGs (Zhang et al. 2022). The gray grids represent model results of PAH band ratios by Rigopoulou et al. (2024) for neutral (top grid), 30% ionized (middle grid), and 70% ionized (bottom grid) PAHs of different sizes (with carbon number  $N_C = 20 - 400$  as marked in order), in the interstellar radiation field (ISRF; the top boundary of each grid) and the  $10^3 \times$  ISRF (the bottom boundary of each grid). Note that the  $3.3 \mu\text{m}$  PAH feature in the nuclear region of NGC 4736 is not detected and the corresponding data point in panel (b) is shown as a faint upper limit with an arbitrary value for illustration purposes.

and also revealed by optical and IR spectroscopy (Davis et al. 2012; Pellegrini et al. 2013; Otter et al. 2024). However, as will be discussed in Section 4, even in the presence of shocks, additional physical conditions, such as a highly obscured environment or a strong AGN radiation, lead to variations in how AGN feedback affects the surrounding material in different galaxies.

### 3.3. PAH Emission Features and Diagnostics

Theoretical calculations show that the size distribution and ionization state of PAH molecules, along with the input radiation field, play a key role in determining the relative strengths of individual PAH features (Draine & Li 2001, 2007; Li & Draine 2001; Maragkoudakis et al. 2020; Draine et al. 2021; Rigopoulou et al. 2021, 2024). Specifically, smaller PAHs, upon absorbing a UV photon, reach much higher excitation levels and consequently radiate at shorter (more energetic) wavelengths because of their low heat capacity. Moreover, when excited, neutral PAHs exhibit stronger C–H bond vibrations responsible for  $3.3$  and  $11.3 \mu\text{m}$  PAH features, whereas cationic PAHs show enhanced C–C bond vibrations that efficiently emit  $6 - 9 \mu\text{m}$  PAH features. Furthermore, a moderately stronger radiation field results in a higher fraction of ionized PAHs, while an FUV-rich (i.e., harder) radiation field enhances the short-wavelength PAH features.

Figure 4 shows that the PAH characteristics in the nuclear regions of the four low-luminosity AGN are distinct from

those of the spatially resolved regions in SFGs (Zhang et al. 2022). This finding clearly demonstrates the influence of AGN feedback, even under the low-excitation conditions prevailing in these low-luminosity AGN (see also Zhang et al. 2022). According to the model results of Rigopoulou et al. (2024), the nuclear regions of NGC 1097, NGC 3190, and NGC 4736 exhibit higher fractions of neutral PAHs with large sizes ( $N_C \gtrsim 200$ ), whereas the nuclear region of NGC 1266 shows a comparable fraction of ionized PAHs to those of SFGs, but with smaller sizes ( $N_C < 20$ ). The PAH characteristics in the nuclear region of NGC 1266 are broadly consistent with those of the highly obscured nuclei in NGC 3256, II Zw 96, and VV 114 presented by Rigopoulou et al. (2024; and references therein). The higher fractions of large, neutral PAHs in the nuclear regions of the other three targets are likely the result of the preferential destruction of the smaller, predominantly ionized PAHs, which are more susceptible to harsh environments surrounding AGN (e.g., Allain et al. 1996b; Micelotta et al. 2010a,b; Holm et al. 2011; García-Bernete et al. 2022a,b, 2024; Zhang et al. 2022, 2024b; Zhang & Ho 2023). The primary cause of the preferential destruction appears to be the shocks discussed above and in the following subsection. Further discussion on the indications of the PAH characteristics in these three targets, also those in NGC 1266, are presented in Section 4.

### 3.4. Warm Molecular Gas Excitation

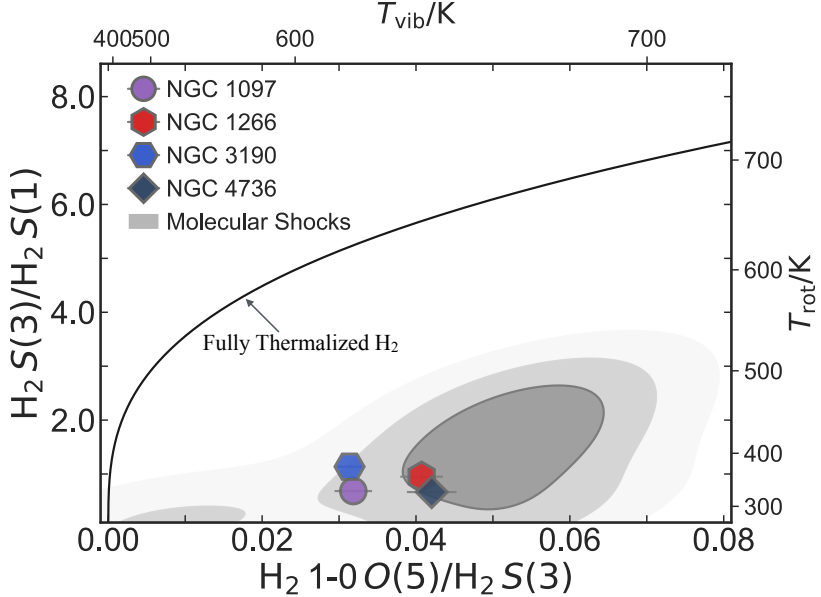


**Figure 5.** Diagnostic diagrams of  $\text{H}_2$  transitions:  $\text{H}_2 \text{ S}(3)/\text{H}_2 \text{ S}(1)$  versus  $\text{H}_2 \text{ 1-0 O}(5)/\text{H}_2 \text{ S}(3)$ , sensitive to  $\text{H}_2$  rotational and vibrational temperatures, respectively. The colored data points represent measurements in the nuclear regions of the four low-luminosity AGN, while the gray contours show the distribution of the best-matched C-type molecular shock model results taken from Kristensen et al. (2023). Additionally, the solid black curve represents the predicted trend of fully thermalized warm  $\text{H}_2$  gas at different temperatures, with the corresponding  $T_{\text{rot}}$  and  $T_{\text{vib}}$  labeled on the right and upper axes, respectively.

Ratios of pure rotational and ro-vibrational transitions from warm ( $\sim 200 - 5000$  K)  $\text{H}_2$  gas are also powerful diagnostics of the excitation mechanisms around AGN, offering key insights into the effects of AGN feedback (e.g., Mouri 1994; Roussel et al. 2007; Mazzalay et al. 2013; Kristensen et al. 2023; López et al. 2025). Figure 5 shows that warm  $\text{H}_2$  gas in the nuclear regions of the four low-luminosity AGN is not fully thermalized, as indicated by the diagnostic ratios  $\text{H}_2 \text{ S}(3)/\text{H}_2 \text{ S}(1)$  and  $\text{H}_2 \text{ 1-0 O}(5)/\text{H}_2 \text{ S}(3)$  lying below the predicted curve for fully thermalized warm  $\text{H}_2$  gas. Specifically, the rotational and vibrational temperatures of fully thermalized warm  $\text{H}_2$  gas are given by  $T_{\text{H}_2} = -\frac{E_i - E_j}{k \ln((\frac{F_i \lambda_i}{A_i g_i}) / (\frac{F_j \lambda_j}{A_j g_j}))}$  (see Equations 1 and 2), using the flux ratios of  $\text{H}_2 \text{ S}(3)/\text{H}_2 \text{ S}(1)$  and  $\text{H}_2 \text{ 1-0 O}(5)/\text{H}_2 \text{ S}(3)$ , and adopting the energy levels and other constants recently calculated by Roueff et al. (2019). Furthermore, as shown by the gray contours in Figure 5, the slow ( $v_s \leq 10 \text{ km s}^{-1}$ ) C-type molecular shocks are plausibly the additional excitation source responsible for the deviation. Specifically, the best-matched molecular shock models are those of Kristensen et al. (2023), characterized by shock velocity  $v_s \leq 10 \text{ km s}^{-1}$ , H atom density  $n_{\text{H}} \leq 10^3 \text{ cm}^{-3}$ , transverse magnetic field scaling factor  $b = 1.0$ , UV field strength  $G_0 = 0$ , PAH abundance  $X(\text{PAH}) = 10^{-6}$ , and  $\text{H}_2$  cosmic-ray excitation rate  $\zeta_{\text{H}_2} = 10^{-15} \text{ s}^{-1}$ . The trend observed in Figure 5 remains when the axes are replaced by the  $\text{H}_2 \text{ S}(5)/\text{H}_2 \text{ S}(1)$  and  $\text{H}_2 \text{ 1-0 O}(7)/\text{H}_2 \text{ S}(5)$  ratios, even though these ratios probe higher

temperatures and require an external UV field for excitation (i.e., the best-matched  $\text{H}_2$  shock models have  $G_0 > 0$ ).

$$T_{\text{rot}} \simeq \frac{-1489}{\ln(0.01748 \times \frac{F_{\text{H}_2 \text{ S}(3)}}{F_{\text{H}_2 \text{ S}(1)}})} \quad (1)$$

$$T_{\text{vib}} \simeq \frac{-4448}{\ln(0.02485 \times \frac{F_{\text{H}_2 \text{ 1-0 O}(5)}}{F_{\text{H}_2 \text{ S}(3)}})} \quad (2)$$

Non-thermal UV heating in photodissociation regions and X-ray heating from AGN are also able to drive warm  $\text{H}_2$  away from full thermalization; however, this is not the case here. Figure 6 presents diagnostic diagrams showing the ratios of the summed  $\text{H}_2 \text{ S}(1)-\text{S}(5)$  emission to the PAH  $7.7 \mu\text{m}$  feature,  $\text{H}_2 \text{ S}(1-5)/\text{PAH}7.7$ , and to the integrated 2–10 keV X-ray emission,  $\text{H}_2 \text{ S}(1-5)/\text{X-ray}(2-10 \text{ keV})$ , plotted against the  $\text{H}_2 \text{ S}(3)/\text{H}_2 \text{ S}(1)$  ratio. The measurements are shown for the nuclear regions of the four low-luminosity AGN and for thirteen  $3'' \times 3''$  apertures sampling the circum-nuclear regions of three higher-luminosity Seyfert galaxies. The corresponding upper limits that can be produced in photodissociation regions (PDRs) and X-ray-dominated regions (XDRs) are indicated by the horizontal dashed lines. Specifically, the upper limits are converted from the corresponding  $\text{H}_2 \text{ S}(0-3)/\text{PAH}7.7$  and  $\text{H}_2 \text{ S}(0-3)/\text{X-ray}(2-10 \text{ keV})$  values (0.04 and 0.01) adopted by Guillard et al. (2012), by multiplying a factor of 0.88. This conversion factor represents the average  $\text{H}_2 \text{ S}(1-5)/\text{H}_2 \text{ S}(0-3)$  ratio predicted by the excitation models of  $\text{H}_2$  gas at temperatures between 100 and

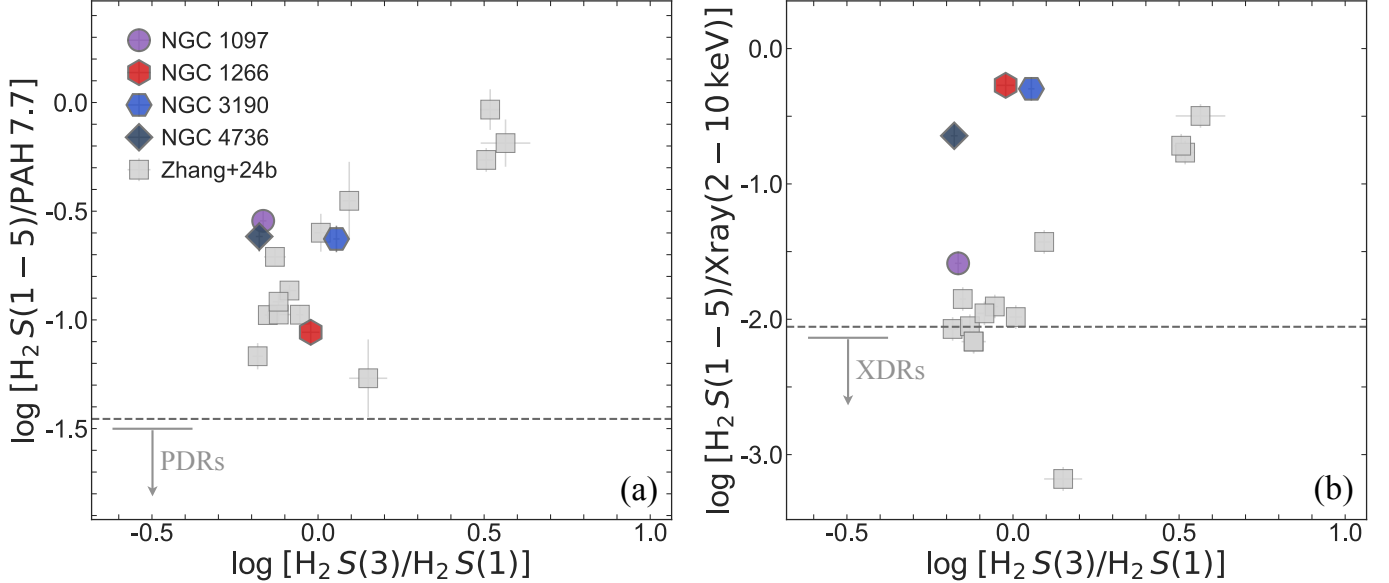


**Figure 6.** Diagnostic diagrams of (a)  $\log [H_2 S(1-5)/PAH 7.7]$  versus  $\log [H_2 S(3)/H_2 S(1)]$  and (b)  $\log [H_2 S(1-5)/X-ray(2-10 \text{ keV})]$  versus  $\log [H_2 S(3)/H_2 S(1)]$ . The colored and gray data points represent measurements for the nuclear regions of the four low-luminosity AGN studied here and in the multiple apertures within the circumnuclear regions of three higher-luminosity Seyferts analyzed by Zhang et al. (2024b), respectively. The horizontal dashed lines in panels (a) and (b) indicate the upper limits of  $H_2 S(1-5)/PAH 7.7$  and  $H_2 S(1-5)/X-ray(2-10 \text{ keV})$  that can be produced in PDRs and XDRs, respectively, as described in the main text (see Section 3.4).

2000 K, calculated by Pereira-Santaella et al. (2014) using RADEX. The  $H_2 S(1-5)/PAH 7.7$  and  $H_2 S(1-5)/X-ray(2-10 \text{ keV})$  ratios in the nuclear regions of the four low-luminosity AGN are all above the upper limits that can be produced in PDRs or XDRs, indicating that non-thermal UV and X-ray heating cannot account for the observed  $H_2$  emission strength and thus further highlighting the impact of the slow molecular shocks. Additionally, as shown by the region with the lowest  $H_2 S(1-5)/X-ray(2-10 \text{ keV})$  values in Figure 6(b), and as will be further discussed in Section 4, X-ray heating appears to play an important role in molecular gas excitation within the nuclear apertures of the higher-luminosity Seyferts that share PAH characteristics similar to those of quasars.

Figure 5 also shows that the warm  $H_2$  gas, mostly traced by low- $J$  pure-rotational transitions, in the nuclear regions of the four low-luminosity AGN does not reach particularly high temperatures. This result is consistent with a higher fraction of the  $H_2$  gas distributed toward the lower-temperature end in these nuclear regions, as indicated by their higher power-law temperature distribution index  $\beta$  ( $\sim 5.0 - 5.5$ ; see Section B), particularly when compared to the nuclear apertures of higher-luminosity Seyferts ( $\beta \approx 4.0 - 5.0$ ; Davies et al. 2024; Zhang et al. 2024b; Delaney et al. 2025). This result further implies that non-thermal heating contributes to the warm  $H_2$  excitation in the nuclear regions of the four low-luminosity AGN. As discussed above, slow molecular shocks are the most likely source of this non-thermal heating, and neither UV heating in PDRs nor X-ray heating from XDRs can account for the observed  $H_2$  emission

strength. Cosmic rays could be another heating source for the warm  $H_2$  (Ferland et al. 2008; Ogle et al. 2010). However, even only for the warm  $H_2$  content in these nuclear regions ( $\sim 10^{4.2} - 10^{6.4} M_{\odot}$ ; see Appendix B), reproducing the observed  $H_2$  fluxes through cosmic-ray heating alone would require cosmic-ray excitation rates of order  $\sim 10^{-11} \text{ s}^{-1}$ , assuming an energy deposition of 20 eV per excitation event and  $\sim 5\%$  of this energy ultimately going to  $H_2$  rotational emission (i.e.,  $L_{H_2}$  is of  $N_{H_2} \times 20 \text{ eV} \times 0.05 \times 10^{-11} \text{ s}^{-1}$ ). The implied cosmic-ray excitation rates are much higher than those expected for low-luminosity AGN ( $\sim 10^{-12} \text{ s}^{-1}$ ; Koutsoumpou et al. 2025a,b), indicating that cosmic-ray heating can only play a secondary role in powering the  $H_2$  rotational emission in these nuclear regions.

In these low-luminosity AGN, molecular shocks, as the most likely heating source for the warm  $H_2$ , are in principle driven by radio jets launched from the nuclear regions (Mukherjee et al. 2018; Meenakshi et al. 2022). Quantitatively, a coupling of only  $\sim 0.1 - 1\%$  of the jet power ( $L_{\text{jet}}$ ) is sufficient to reproduce the observed  $H_2$  fluxes in most of these nuclear regions. The exception is NGC 1266, which requires a coupling of  $\sim 4\%$ . To estimate  $L_{\text{jet}}$ , we adopt the empirical correlation between  $L_{\text{jet}}$  and  $L_{1.4\text{GHz}}^{\text{radio}}$  described by Heckman & Best (2014; Equation 1 therein with  $f_W = 15$ ). The estimated couplings remain largely unchanged when using the updated  $L_{\text{jet}}$  calibration provided by Roy et al. (2025; Equation 5 therein). Interestingly, the coupling efficiencies estimated here for the warm  $H_2$  emission are comparable to those inferred for ionized gas outflows in high-redshift radio

galaxies (< 1%; Roy et al. 2025) and in NGC 1266 ( $\sim 4\%$ ; Nyland et al. 2013). This result further highlights the important and multifaceted roles played by the radio (kinetic) mode AGN feedback in galaxy evolution.

#### 4. DISCUSSION: INSIGHTS INTO AGN FEEDBACK MECHANISMS

PAHs in space are not a single, homogeneous population but instead span a broad molecular size distribution, with carbon number of  $\sim 10 - 1000$  (e.g., Li & Draine 2001; Weingartner & Draine 2001; Draine et al. 2021). Broadly speaking, the size distribution and ionization stage of PAH population in space are governed by their formation and subsequent processing, and variations in the observed PAH band ratios therefore reflect the underlying physical processes acting on PAH population. PAHs can form via both “bottom-up” pathways, in which PAHs grow from smaller molecules (e.g., Frenklach & Feigelson 1989; Cherchneff et al. 1992; and see the review by Reizer et al. 2022), and “top-down” pathways, in which PAHs are produced through the fragmentation of larger grains (e.g., Jones et al. 1996; Scott et al. 1997; Raj et al. 2014; Hirashita & Aoyama 2019; Hirashita & Murga 2020). Subsequent PAH processing includes photo-processing (e.g., Jochims et al. 1994; Allain et al. 1996a; Holm et al. 2011) and shock-processing (e.g., Jones et al. 1996; Micelotta et al. 2010a,b). Consequently, by combining emission models for individual PAH sub-populations, analyses of variations in observed PAH band ratios can provide insight into the physical processes governing PAH formation and processing in different environments. To this end, Figure 7 revisits the widely used PAH band-ratio diagram, incorporating additional PAH measurements from the literature to sample a broad range of PAH band ratios and, in turn, the underlying physical conditions. Note that the additional PAH measurements come from diverse galactic environments observed with comparable arcsec-scale aperture sizes but were derived using the same profile-fitting methodology, ensuring a consistent and systematic comparison.

The literature PAH measurements compiled here are not intended to be exhaustive across all galactic systems, but rather to sample typical star-forming and AGN central regions, along with a few distinctive environments that exhibit unusual PAH characteristics, in order to illustrate the sensitivity of PAH features to differing physical conditions, as reflected in their distinct overall PAH band ratios. Accordingly, the added galactic systems span spatially resolved regions from the central areas of SINGS SFGs and AGN (including both LINERs and Seyferts; Zhang et al. 2022), central-region observations from a larger set of AGN (most are Seyferts; Smith et al. 2007; O’Dowd et al. 2009; Diamond-Stanic & Rieke 2010; Gallimore et al. 2010; Sales et al. 2010; García-Bernete et al. 2022b), low-redshift quasars (Xie & Ho 2022),

low-metallicity blue compact dwarf galaxies (BCDs; Hunt et al. 2010; Lebouteiller et al. 2011), local giant H II regions in NGC 3603 (in the Milky Way), 30 Doradus (in the Large Magellanic Cloud), and N 66 (in the Small Magellanic Cloud) (Lebouteiller et al. 2011), as well as multiple apertures within the circumnuclear regions of three Seyferts with JWST spectroscopy (Zhang et al. 2024b), and highly obscured nuclei with JWST spectroscopy (Rigopoulou et al. 2024). As noted above, the distinct distributions of these galactic systems on the PAH diagram plausibly arise from differing feedback effects that regulate the interstellar medium (ISM) properties. Despite the distinct PAH characteristics, their connection through the SFG and AGN measurements hints at a more continuous and interconnected evolutionary pathway of the ISM and, consequently, of galaxies. The following discussion provides a more comprehensive view of the feedback effects, especially those in AGN, by integrating the information conveyed by the PAH characteristics and other diagnostics discussed above for these galactic systems.

SFGs exhibit similar PAH characteristics, as evidenced by the concentrated distribution of the spatially resolved regions in SFGs in Figure 7, and thus serve as a useful baseline for highlighting the effects of different feedback mechanisms. Within the clustered distribution, the PAH characteristics of SFG regions are primarily regulated by the strength and hardness of their radiation fields (Zhang et al. 2022). Specifically, Zhang et al. (2022) found that the average PAH  $6.2 \mu\text{m}/7.7 \mu\text{m}$  ratio of SFG regions increases with increasing  $[\text{Ne III}]/[\text{Ne II}]$ , an indicator of radiation field hardness (e.g., Thornley et al. 2000; Förster Schreiber et al. 2001), while the average PAH  $11.3 \mu\text{m}/7.7 \mu\text{m}$  ratio first decreases with  $[\text{Ne III}]/[\text{Ne II}]$  and then the trend reverses. The first decrease of PAH  $11.3 \mu\text{m}/7.7 \mu\text{m}$  ratio is consistent with a higher fraction of ionized PAHs and enhanced short-wavelength PAH features in a moderately strong, hard radiation field. Additionally, Zhang et al. (2022) proposed that an excessively strong and hard radiation field causes selective photo-erosion and subsequent photo-destruction of PAHs, primarily the ionized ones, shifting the PAH size distribution toward smaller and more neutral molecules (the “top-down” scenario). These photo-processing effects explain the final increase of both PAH  $6.2 \mu\text{m}/7.7 \mu\text{m}$  and PAH  $11.3 \mu\text{m}/7.7 \mu\text{m}$  ratios along the direction toward the distribution of the low-metallicity BCDs and local giant H II regions in Figure 7.

Following the trend seen in SFGs, the photo-processing effects in the even stronger and harder radiation fields of low-metallicity BCDs and local giant H II regions at least partially explain their on average large values of both PAH  $6.2 \mu\text{m}/7.7 \mu\text{m}$  and PAH  $11.3 \mu\text{m}/7.7 \mu\text{m}$  ratios. Furthermore, as detailed by Whitcomb et al. (2024, 2025), the in-

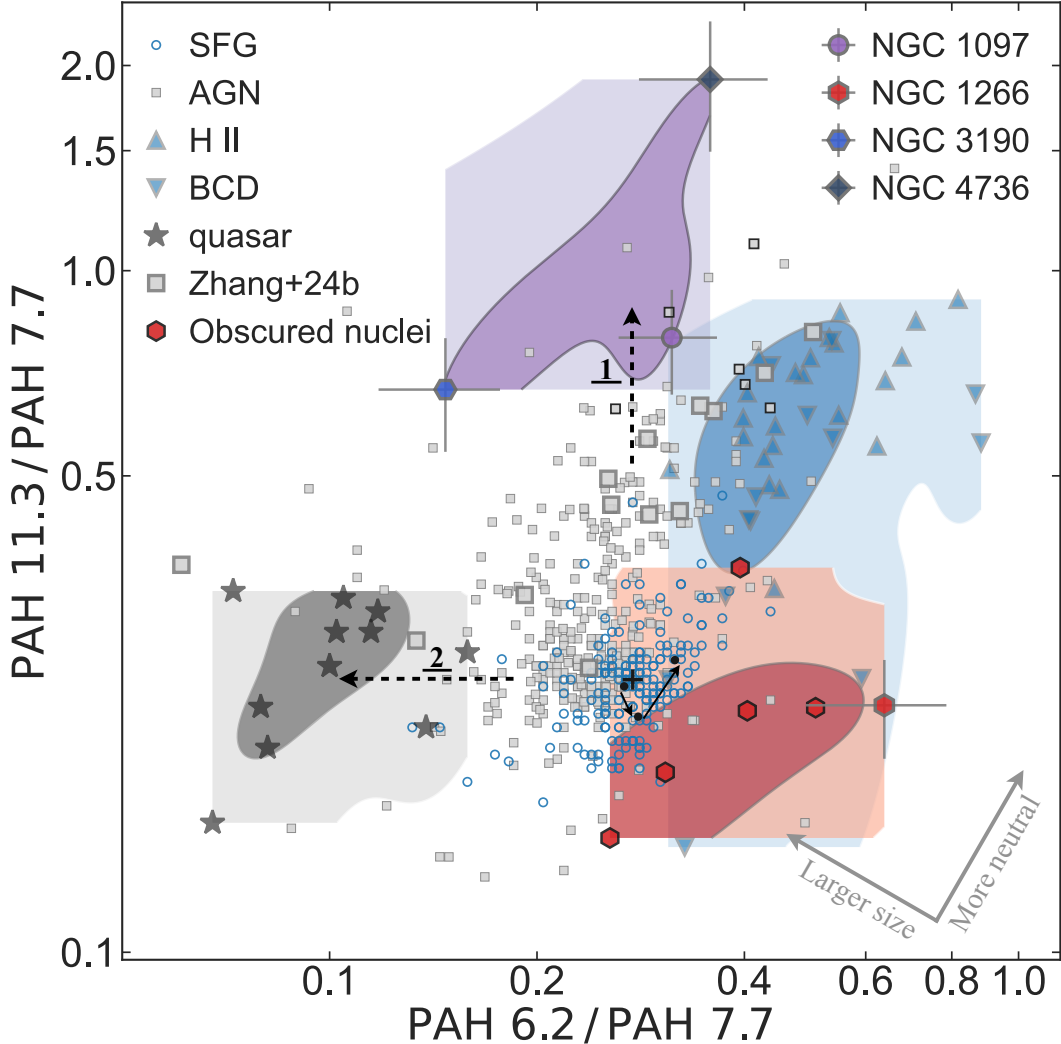


**Figure 7.** The same PAH band ratio diagram as Figure 4(a), but including additional data points compiled from the literature. Blue circles: the distribution of PAH band ratios of spatially resolved regions in SINGS SFGs (Zhang et al. 2022), with the black plus representing the median value of all SFG regions and the black dots (from left to right) indicating the median values of SFG regions with  $\log [\text{Ne III}]/[\text{Ne II}] < -0.7$ ,  $-0.7 \leq \log [\text{Ne III}]/[\text{Ne II}] \leq -0.5$ , and  $\log [\text{Ne III}]/[\text{Ne II}] > -0.5$ , respectively. Small gray squares: PAH band ratios of spatially resolved circumnuclear regions in SINGS AGN, and central regions of a larger set of AGN. The small gray squares further outlined in black are Seyfert central regions with the most pronounced  $\text{H}_2$  emission in Diamond-Stanic & Rieke (2010). Gray stars: PAH band ratios of low-redshift quasars detected in all the three PAH features. Blue triangles: PAH band ratios of low-metallicity BCDs and local giant H II regions. Large gray squares: PAH band ratios of the multiple apertures sampling the circumnuclear regions of three Seyferts as also shown in Figure 6 (Zhang et al. 2024b). Red hexagons: PAH band ratios of highly obscured nuclei studied by Rigopoulou et al. (2024), together with the nuclei of NGC 1266 analyzed here. Other markers: the nuclei of the other three low-luminosity AGN analyzed in this work. Dashed black arrows: the two potential branches of AGN feedback (1: kinetic mode; 2: radiative mode). Gray arrows in the lower-right: the directions in theory of increasing overall PAH size and neutral fraction as the PAH band ratios change. Colored contours: the density contours of the overall distributions of different galactic environments. Note that the PAH band ratios from Rigopoulou et al. (2024), Zhang et al. (2024b), and this work were obtained from higher-spatial-resolution JWST/MRS spectroscopy, whereas those from the other studies shown here are based on Spitzer/IRS spectroscopy.

hibited growth of PAHs, which successfully reproduces the relatively elevated (but absolutely declined) fraction of the smallest PAHs among the overall PAH population in the low-metallicity environments, can further explain the distribution of these BCDs and H II regions (the “bottom up” scenario). The selective erosion and the inhibited growth of PAHs may

also apply to the highly obscured nuclei in Figure 7, given their elevated fractions of smaller PAHs. However, in these highly obscured nuclei, scenarios involving the selective erosion of larger PAHs, or, alternatively, the enhanced production of smaller PAHs through fragmentation of large grains, are particularly favored, as evidenced by their not only rela-

tively but also absolutely stronger PAH  $3.3\text{ }\mu\text{m}$  feature predominantly tracing the smallest PAH population. Specifically, NGC 1266 nucleus exhibits strong absorption features from organic residues around  $7.42$  and  $7.674\text{ }\mu\text{m}$ . The cold, dense environments in these highly obscured nuclei provide the ideal physical conditions for dust growth and molecular synthesis (see review [Herbst & van Dishoeck 2009](#)). The highly obscured, ice-rich environments may also protect ionized PAHs from photo-destruction (e.g., [Alonso-Herrero et al. 2014, 2020; García-Bernete et al. 2022b, 2025](#)), explaining the large fraction of very small yet ionized PAHs observed therein. Also notably, the host galaxies of these highly obscured nuclei exhibit peculiar morphologies, indicative of gravitational interactions capable of channeling molecular gas toward their nuclei. We thus suspect that the molecular shocks responsible for the enhanced  $\text{H}_2$  emission and the associated selective erosion/fragmentation of PAHs may be the relics of past gravitational encounters.

In contrast to the concentrated distribution of SFG regions, AGN central regions occupy a much broader distribution of PAH band ratios, displaying characteristically larger  $11.3\text{ }\mu\text{m}/7.7\text{ }\mu\text{m}$  but smaller  $6.2\text{ }\mu\text{m}/7.7\text{ }\mu\text{m}$  toward two potential branches. The PAH characteristics observed in AGN can be attributed to the destruction of smaller, predominantly ionized PAHs by feedback effects, though the underlying mechanisms appear to differ between low- and high-luminosity AGN. As detailed in Section 3, in low-luminosity AGN toward the *vertical* branch, the feedback mechanism responsible for the destruction is most likely shock-driven, associated with the kinetic mode feedback (see also [Zhang et al. 2022](#)). However, in low-redshift quasars toward the *horizontal* branch, photo-destruction by their intense radiation fields is favored given that these systems are dominated by radiative-mode feedback. In line with the latter point, the higher-luminosity Seyferts whose nuclear apertures show non-negligible X-ray heating of the molecular gas as shown by Figure 6(b) also exhibit PAH characteristics similar to those of the quasars in Figure 7 (see more discussion in [Zhang et al. 2024b](#)). Moreover, X-ray photons penetrate much deeper into molecular gas than UV photons, allowing them to irradiate and excite large PAH molecules that would otherwise remain neutral. As a result, the surviving large PAHs in quasars are predominantly ionized, whereas those in most Seyferts remain mostly neutral. For other AGN central regions that lie between the SFG loci and those of low-luminosity AGN and quasars, a combination of shocks, intense AGN radiation, and star formation, may be required to explain their PAH characteristics. This interpretation is particularly relevant for AGN central regions observed with larger apertures, or for obscured AGN where host-galaxy inclination or a dense nuclear gas disk contributes to the observed properties. More importantly, although based on

a modest sample of low-luminosity AGN, the preliminary analysis suggests that SFG regions, low-luminosity AGN, and quasars collectively form a useful set of anchor points for assessing the relative influence of different AGN feedback modes through a mixing-sequence PAH diagram. A more rigorous quantitative analysis will require spatially resolved JWST spectroscopy of an expanded AGN sample, particularly at the low-luminosity end.

Another noteworthy result in Figure 7 is that the nuclear apertures of higher-luminosity Seyferts with the most pronounced  $\text{H}_2$  emission, an indicator of shocks, in Figure 6, as well as the central regions of Seyferts with the most pronounced  $\text{H}_2$  emission in [Diamond-Stanic & Rieke \(2010\)](#), occupy a region between the low-luminosity AGN and low-metallicity environments. Most of these Seyferts also exhibit peculiar morphologies and could be analogs of the above highly obscured nuclei, but with higher AGN luminosities (though still below those dominated by X-ray photo-processing effects). If this supposition is correct, the distribution of these Seyferts with stronger signatures of molecular shocks and a relatively higher fraction of small PAHs could result from the competition between different feedback effects. These effects include the selective erosion/fragmentation of larger PAH grains, producing more smaller PAHs (as seen in the highly obscured nuclei), and the complete destruction of smaller PAHs, either by shocks (as in the nuclear regions of the low-luminosity AGN) or by the AGN radiation (as in quasars). Galactic systems that exhibit signatures of both AGN activity and gravitational interactions, such as some ultraluminous infrared galaxies (ULIRGs), will be ideal laboratories to test this idea in future studies.

## 5. SUMMARY AND CONCLUSIONS

Leveraging high quality JWST NIRSpec/IFU and MIRI/MRS spectroscopy obtained as an extension of the Galaxy Activity, Torus, and Outflow Survey (GATOS), this letter presents the distinct emission properties of ionized gas, PAHs, and  $\text{H}_2$  in the nuclear ( $r < 150\text{ pc}$ ) regions of a sample of four low-luminosity AGN. We find that these low-luminosity AGN exhibit much weaker high-ionization potential lines (e.g.,  $[\text{Ne V}]$  and  $[\text{O IV}]$ ) compared to higher-luminosity Seyferts, and have emission line ratios indicative of fast radiative shocks (with  $v_s$  of  $\sim 100\text{s km s}^{-1}$ ) as the primary excitation source of ionized gas therein (Section 3.2). Despite their low-excitation conditions, their PAH characteristics point to a critical role of AGN feedback in regulating the ISM properties of these low-luminosity AGN (Section 3.3). Furthermore, the  $\text{H}_2$  gas in these low-luminosity AGN are not fully thermalized, with slow, plausibly jet-driven molecular shocks (with  $v_s \leq 10\text{ km s}^{-1}$ ) likely responsible for its excitation. The role of molecular shocks is

further supported by the fact that non-thermal UV, X-ray, and cosmic-ray heating are all insufficient to explain the observed H<sub>2</sub> emission strength, whereas radio jets with a coupling efficiency of  $\sim 0.1 - 4\%$  can reproduce the observed H<sub>2</sub> fluxes in these nuclear regions. (Section 3.4).

Taken together with results from the literature, we specifically discussed the underlying mechanisms responsible for the widely distributed PAH band ratios observed across different galactic systems, particularly among AGN of varying luminosities (Section 4). The main points of the discussion can be summarized as follows:

1. In SFGs, a moderately strong and hard radiation field leads to a higher fraction of ionized PAHs and enhanced emission features at short wavelengths, whereas an excessively strong and hard radiation field causes selective photo-erosion and subsequent photo-destruction of PAHs, shifting the PAH size distribution toward relatively smaller and more neutral molecules.
2. In AGN, feedback effects tend to destroy smaller, predominantly ionized PAHs, though the underlying mechanisms differ with AGN luminosity. In low-luminosity AGN, the destruction is likely driven by shocks associated with the prevalent kinetic-mode feedback therein, whereas in quasars that are dominated by radiative-mode feedback, photo-destruction by the intense AGN radiation is favored. For most AGN, the mixed effect of shocks and AGN radiation fields is required.
3. Certain galactic systems such as low-metallicity BCDs and local giant H II regions, highly obscured nuclei, and some Seyferts exhibiting the most prominent H<sub>2</sub> emission, appear to contain an elevated fraction of smaller PAHs, either ionized or neutral depending on the physical conditions. The underlying processes responsible for the production of these smaller PAHs involve photo-processing, inhibited grain growth, enhanced PAH formation, or the combination thereof.

Although based on a modest sample, our analysis of the infrared ( $\sim 3 - 28 \mu\text{m}$ ) spectra indicates that shocks (i.e., the kinetic mode feedback) play a central role in shaping the nuclear environments of low-luminosity AGN. More-

over, SFGs, low-luminosity AGN, and quasars together provide a useful set of anchor points for assessing the relative influence of different AGN feedback modes through a mixing-sequence PAH diagram. A more robust, quantitative analysis will require further spatially resolved analysis and JWST spectroscopy of an expanded AGN sample in future cycles, particularly at the low-luminosity end, as well as distinctive systems such as Seyferts with strong H<sub>2</sub> emission and ULIRGs exhibiting signatures of both AGN activity and gravitational interactions.

## ACKNOWLEDGMENTS

We thank the anonymous referee for detailed comments and suggestions to improve the presentation of our results and corresponding discussions. This letter is part of a series from the [Galaxy Activity, Torus, and Outflow Survey \(GATOS\)](#) collaboration. LZ and CP acknowledge grant support from the Space Telescope Science Institute (ID: JWST-GO-01670; JWST-GO-03535; JWST-GO-04225; JWST-GO-04972). EKSH and DD acknowledge support from the NASA Astrophysics Data Analysis Program (22-ADAP22-0173). MPS acknowledges support from grants RYC2021-033094-I, CNS2023-145506, and PID2023-146667NB-I00 funded by MCIN/AEI/10.13039/501100011033 and the European Union NextGenerationEU/PRTR. CR acknowledges support from SNSF Consolidator grant F01-13252, Fondecyt Regular grant 1230345, ANID BASAL project FB210003 and the China-Chile joint research fund. AAH and LHM acknowledge financial support by the grant PID2021-124665NB-I00 funded by MCIN/AEI/10.13039/501100011033 and ERDF A way of making Europe. IGB is supported by the Programa Atracción de Talento Investigador “César Nombela” via grant 2023-T1/TEC-29030 funded by the Community of Madrid. EB acknowledges support from the Spanish grants PID2022-138621NB-I00 and PID2021-123417OB-I00, funded by MCIN/AEI/10.13039/501100011033/FEDER, EU. SFH acknowledges support through UK Research and Innovation (UKRI) under the UK government’s Horizon Europe Funding Guarantee (EP/Z533920/1, selected in the 2023 ERC Advanced Grant round) and an STFC Small Award (ST/Y001656/1).

## REFERENCES

Alatalo, K., Lacy, M., Lanz, L., et al. 2015, *ApJ*, 798, 31  
 Alatalo, K., Nyland, K., Graves, G., et al. 2014, *ApJ*, 780, 2, 186  
 Allain, T., Leach, S., & Sedlmayr, E. 1996a, *A&A*, 305, 602  
 Allain, T., Leach, S., & Sedlmayr, E. 1996b, *A&A*, 305, 616

Alonso Herrero, A., Hermosa Muñoz, L., Labiano, A., et al. 2025, *A&A*, 699, A334  
 Alonso-Herrero, A., Pereira-Santaella, M., Rigopoulou, D., et al. 2020, *A&A*, 639, A43

Alonso-Herrero, A., Ramos Almeida, C., Esquej, P., et al. 2014, MNRAS, 443, 2766

Argyriou, I., Glasse, A., Law, D. R., et al. 2023, A&A, 675, A111

Argyriou, I., Wells, M., Glasse, A., et al. 2020, A&A, 641, A150

Armus, L., Charmandaris, V., Bernard-Salas, J., et al. 2007, ApJ, 656, 148

Armus, L., Lai, T., U, V., et al. 2023, ApJL, 942, 2, L37

Böker, T., Arribas, S., Lützgendorf, N., et al. 2022, A&A, 661, A82

Boogert, A. C. A., Gerakines, P. A., & Whittet, D. C. B. 2015, ARA&A, 53, 541

Bushouse, H., Eisenhamer, J., Dencheva, N., et al. 2025, Zenodo, 1.18.0. doi:10.5281/zenodo.15178003

Ceci, M., Marconcini, C., Marconi, A., et al. 2025, A&A submitted, arXiv:2507.08077

Chen, P., Zhao, Y., & Wang, J. 2023, Research in Astronomy and Astrophysics, 23, 015005

Cherchneff, I., Barker, J. R., & Tielens, A. G. G. M. 1992, ApJ, 401, 269

Chown, R., Sidhu, A., Peeters, E., et al. 2024, A&A, 685, A75

Cisternas, M., Gadotti, D. A., Knapen, J. H., et al. 2013, ApJ, 776, 50

Dale, D. A., Smith, J. D. T., Armus, L., et al. 2006, ApJ, 646, 1, 161

Davé, R., Anglés-Alcázar, D., Narayanan, D., et al. 2019, MNRAS, 486, 2827

Davé, R., Crain, R. A., Stevens, A. R. H., et al. 2020, MNRAS, 497, 146

Davies, R., Shimizu, T., Pereira-Santaella, M., et al. 2024, A&A, 689, A263

Davis, T. A., Krajnović, D., McDermid, R. M., et al. 2012, MNRAS, 426, 2, 1574

Delaney, D. E., Hicks, E. K. S., Zhang, L., et al. 2025, ApJ, 993, 217

Di Matteo, T., Allen, S. W., Fabian, A. C., et al. 2003, ApJ, 582, 133

Di Matteo, T., Springel, V., & Hernquist, L. 2005, Nature, 433, 604

Diamond-Stanic, A. M. & Rieke, G. H. 2010, ApJ, 724, 140

Donnan, F. R., García-Bernete, I., Rigopoulou, D., et al. 2023, MNRAS, 519, 3691

Donnelly, G. P., Smith, J. D. T., Draine, B. T., et al. 2024, ApJ, 965, 1, 75

Draine, B. T. & Li, A. 2001, ApJ, 551, 2, 807

Draine, B. T. & Li, A. 2007, ApJ, 657, 810

Draine, B. T., Li, A., Hensley, B. S., et al. 2021, ApJ, 917, 1, 3

Draine, B. T., Sandstrom, K., Dale, D. A., et al. 2025, ApJL, 984, 2, L42

Fabian, A. C. 2012, ARA&A, 50, 455

Farrah, D., Bernard-Salas, J., Spoon, H. W. W., et al. 2007, ApJ, 667, 149

Feltre, A., Gruppioni, C., Marchetti, L., et al. 2023, A&A, 675, A74

Ferland, G. J., Fabian, A. C., Hatch, N. A., et al. 2008, MNRAS, 386, 1, L72

Fernández-Ontiveros, J. A., López-López, X., & Prieto, A. 2023, A&A, 670, A22

Ferrarese, L. & Merritt, D. 2000, ApJL, 539, L9

Förster Schreiber, N. M., Genzel, R., Lutz, D., et al. 2001, ApJ, 552, 2, 544

Forbes, D. A. & Ward, M. J. 1993, ApJ, 416, 150

Frenklach, M. & Feigelson, E. D. 1989, ApJ, 341, 372

Gallimore, J. F., Yzaguirre, A., Jakoboski, J., et al. 2010, ApJS, 187, 172

Gasman, D., Argyriou, I., Sloan, G. C., et al. 2023, A&A, 673, A102

Gebhardt, K., Bender, R., Bower, G., et al. 2000, ApJL, 539, L13

García-Bernete, I., Donnan, F. R., Rigopoulou, D., et al. 2025, A&A, 696, A135

García-Bernete, I., Rigopoulou, D., Alonso-Herrero, A., et al. 2022a, A&A, 666, L5

García-Bernete, I., Rigopoulou, D., Alonso-Herrero, A., et al. 2022b, MNRAS, 509, 4256

García-Bernete, I., Rigopoulou, D., Donnan, F. R., et al. 2024, A&A, 691, A162

Gardner, J. P., Mather, J. C., Abbott, R., et al. 2023, PASP, 135, 068001

Genzel, R., Lutz, D., Sturm, E., et al. 1998, ApJ, 498, 579

González-Martín, O., Díaz-González, D. J., Martínez-Paredes, M., et al. 2025, MNRAS, 539, 3, 2158

González-Martín, O., Masegosa, J., Márquez, I., et al. 2015, A&A, 578, A74

Goold, K., Seth, A., Molina, M., et al. 2024, ApJ, 966, 2, 204

Gordon, K. D., Engelbracht, C. W., Rieke, G. H., et al. 2008, ApJ, 682, 336

Greene, J. E., Strader, J., & Ho, L. C. 2020, ARA&A, 58, 257

Guillard, P., Ogle, P. M., Emonts, B. H. C., et al. 2012, ApJ, 747, 2, 95

Harrison, C. M. & Ramos Almeida, C. 2024, Galaxies, 12, 2, 17

Harrison, C. M., Alexander, D. M., Mullaney, J. R., et al. 2014, MNRAS, 441, 4, 3306

Heckman, T. M. & Best, P. N. 2014, ARA&A, 52, 589

Heckman, T. M. 1980, A&A, 87, 152

Herbst, E. & van Dishoeck, E. F. 2009, ARA&A, 47, 1, 427

Hermosa Muñoz, L., Alonso-Herrero, A., Pereira-Santaella, M., et al. 2024, A&A, 690, A350

Hermosa Muñoz, L., Alonso-Herrero, A., Labiano, A., et al. 2025a, A&A, 693, A321

Hermosa Muñoz, L., González Fernández, J. R., Alonso-Herrero, A., et al. 2025b, A&A submitted, arXiv:2509.14019

Hernandez, S., Jones, L., Smith, L. J., et al. 2023, ApJ, 948, 2, 124

Hirashita, H. & Aoyama, S. 2019, MNRAS, 482, 2, 2555

Hirashita, H. & Murga, M. S. 2020, MNRAS, 492, 3, 3779

Ho, L. C. 1999, ApJ, 516, 672

Ho, L. C. 2008, ARA&A, 46, 475

Ho, L. C. 2009, ApJ, 699, 626

Ho, L. C., Greene, J. E., Filippenko, A. V., et al. 2009, ApJS, 183, 1

Ho, L. C., Filippenko, A. V., & Sargent, W. L. W. 1993, ApJ, 417, 63

Ho, L. C., Filippenko, A. V., & Sargent, W. L. W. 2003, ApJ, 583, 159

Holm, A. I. S., Johansson, H. A. B., Cederquist, H., et al. 2011, JChPh, 134, 044301

Hopkins, P. F., Cox, T. J., Kereš, D., et al. 2008b, ApJS, 175, 390

Hopkins, P. F., Hernquist, L., Cox, T. J., et al. 2008a, ApJS, 175, 356

Hopkins, P. F., Hernquist, L., Cox, T. J., et al. 2006, ApJS, 163, 1

Hunt, L. K., Draine, B. T., Navarro, M. G., et al. 2025, ApJ, 993, 1, 84

Hunt, L. K., Thuan, T. X., Izotov, Y. I., et al. 2010, ApJ, 712, 164

Ilha, G. S., Harrison, C. M., Mainieri, V., et al. 2025, A&A, 704, A293

Jakobsen, P., Ferruit, P., Alves de Oliveira, C., et al. 2022, A&A, 661, A80

Jochims, H. W., Ruhl, E., Baumgartel, H., et al. 1994, ApJ, 420, 307

Jones, A. P., Tielens, A. G. G. M., & Hollenbach, D. J. 1996, ApJ, 469, 740

Kaneda, H., Onaka, T., & Sakon, I. 2005, ApJL, 632, L83

Kennicutt, R. C., Armus, L., Bendo, G., et al. 2003, PASP, 115, 928

Koo, B.-C., Raymond, J. C., & Kim, H.-J. 2016, Journal of Korean Astronomical Society, 49, 3, 109

Kormendy, J. & Ho, L. C. 2013, ARA&A, 51, 511

Koutsoumpou, E., Fernández-Ontiveros, J. A., Dasyra, K. M., et al. 2025a, A&A, 693, A215

Koutsoumpou, E., Fernández-Ontiveros, J. A., Dasyra, K. M., et al. 2025b, A&A 704, A26

Kristensen, L. E., Godard, B., Guillard, P., et al. 2023, A&A, 675, A86

Lai, T. S.-Y., Armus, L., Bianchin, M., et al. 2023, ApJL, 957, 2, L26

Lai, T. S.-Y., Smith, J. D. T., Baba, S., et al. 2020, ApJ, 905, 1, 55

Law, D. R., E. Morrison, J., Argyriou, I., et al. 2023, AJ, 166, 45

Lebouteiller, V., Bernard-Salas, J., Whelan, D. G., et al. 2011, ApJ, 728, 45

Li, A. & Draine, B. T. 2001, ApJ, 554, 2, 778

López, I. E., Bertola, E., Reynaldi, V., et al. 2025, 994, 206

Magorrian, J., Tremaine, S., Richstone, D., et al. 1998, AJ, 115, 2285

Maragkoudakis, A., Peeters, E., & Ricca, A. 2020, MNRAS, 494, 1, 642

Mason, R. E., Lopez-Rodriguez, E., Packham, C., et al. 2012, AJ, 144, 11

Mazzalay, X., Saglia, R. P., Erwin, P., et al. 2013, MNRAS, 428, 3, 2389

McNamara, B. R. & Nulsen, P. E. J. 2007, ARA&A, 45, 117

Meenakshi, M., Mukherjee, D., Wagner, A. Y., et al. 2022, MNRAS, 516, 1, 766

Mezcua, M. & Prieto, M. A. 2014, ApJ, 787, 1, 62

Micelotta, E. R., Jones, A. P., & Tielens, A. G. G. M. 2010a, A&A, 510, A36

Micelotta, E. R., Jones, A. P., & Tielens, A. G. G. M. 2010b, A&A, 510, A37

Mouri, H. 1994, ApJ, 427, 777

Mouri, H., Kawara, K., & Taniguchi, Y. 2000, ApJ, 528, 1, 186

Moustakas, J., Kennicutt, R. C., Tremonti, C. A., et al. 2010, ApJS, 190, 2, 233

Mukherjee, D., Bicknell, G. V., Wagner, A. Y., et al. 2018, MNRAS, 479, 4, 5544

Nagar, N. M., Falcke, H., & Wilson, A. S. 2005, A&A, 435, 2, 521

Nagar, N. M., Falcke, H., Wilson, A. S., et al. 2002, A&A, 392, 53

Nemmen, R. S., Storchi-Bergmann, T., & Eracleous, M. 2014, MNRAS, 438, 4, 2804

Nemmen, R. S., Storchi-Bergmann, T., Yuan, F., et al. 2006, ApJ, 643, 2, 652

Nesvadba, N. P. H., De Breuck, C., Lehnert, M. D., et al. 2017, A&A, 599, A123

Nyland, K., Alatalo, K., Wrobel, J. M., et al. 2013, ApJ, 779, 2, 173

O'Dowd, M. J., Schiminovich, D., Johnson, B. D., et al. 2009, ApJ, 705, 885

Ogle, P., Boulanger, F., Guillard, P., et al. 2010, ApJ, 724, 2, 1193

Ogle, P. M., Sebastian, B., Aravindan, A., et al. 2025, ApJ, 983, 2, 98

Otter, J. A., Alatalo, K., Rowlands, K., et al. 2024, ApJ, 975, 1, 142

Raj, A., Tayouo, R., Cha, D., et al. 2014, Combust. Flame 161 (9), 2446–2457. <https://doi.org/10.1016/J.COMBUSTFLAME.2014.02.010>.

Ramos Almeida, C., García-Bernete, I., Pereira-Santaella, M., et al. 2025, A&A, 698, A194

Roueff, E., Abgrall, H., Czachorowski, P., et al. 2019, A&A, 630, A58

Padovani, P., Alexander, D. M., Assef, R. J., et al. 2017, A&A Rv, 25, 2

Pillepich, A., Springel, V., Nelson, D., et al. 2018, MNRAS, 473, 4077

Peeters, E., Habart, E., Berné, O., et al. 2024, A&A, 685, A74

Peeters, E., Hony, S., Van Kerckhoven, C., et al. 2002, A&A, 390, 1089

Pellegrini, E. W., Smith, J. D., Wolfire, M. G., et al. 2013, ApJL, 779, 2, L19

Pellegrini, S., Venturi, T., Comastri, A., et al. 2003, ApJ, 585, 677

Pereira-Santaella, M., Álvarez-Márquez, J., García-Bernete, I., et al. 2022, *A&A*, 665, L11

Pereira-Santaella, M., Diamond-Stanic, A. M., Alonso-Herrero, A., et al. 2010, *ApJ*, 725, 2270

Pereira-Santaella, M., Rigopoulou, D., Farrah, D., et al. 2017, *MNRAS*, 470, 1218

Pereira-Santaella, M., Spinoglio, L., van der Werf, P. P., et al. 2014, *A&A*, 566, A49

Pontoppidan, K. M., Salyk, C., Banzatti, A., et al. 2024, *ApJ*, 963, 2, 158

Reizer, E., Viskolcz, B., & Fiser, B. 2022, *Chemosphere*, 291, 132793

Riffel, R. A., Colina, L., Costa-Souza, J. H., et al. 2025, *A&A* in press, arXiv:2510.02517

Rigopoulou, D., Barale, M., Clary, D. C., et al. 2021, *MNRAS*, 504, 4, 5287

Rigopoulou, D., Donnan, F. R., García-Bernete, I., et al. 2024, *MNRAS*, 532, 2, 1598

Roussel, H., Helou, G., Hollenbach, D. J., et al. 2007, *ApJ*, 669, 2, 959

Roy, N., Heckman, T., & Henry, A. 2025, *ApJ* submitted, arXiv:2508.06707

Sales, D. A., Pastoriza, M. G., & Riffel, R. 2010, *ApJ*, 725, 605

Schaye, J., Crain, R. A., Bower, R. G., et al. 2015, *MNRAS*, 446, 521

Scott, A., Duley, W. W., & Pinho, G. P. 1997, *ApJL*, 489, L193

Smith, J. D. T., Draine, B. T., Dale, D. A., et al. 2007, *ApJ*, 656, 770

Shajib, A. J., Treu, T., Melo, A., et al. 2025, *A&A*, 702, L12

Spinoglio, L. & Malkan, M. A. 1992, *ApJ*, 399, 504

Sutherland, R. S. & Dopita, M. A. 2017, *ApJS*, 229, 34

Thornley, M. D., Förster Schreiber, N. M., Lutz, D., et al. 2000, *ApJ*, 539, 641

Togi, A. & Smith, J. D. T. 2016, *ApJ*, 830, 18

Vayner, A., Díaz-Santos, T., Eisenhardt, P. R. M., et al. 2025, *ApJ*, 989, 2, 230

Wang, W., Wylezalek, D., De Breuck, C., et al. 2024, *A&A*, 683, A169

Weinberger, R., Springel, V., Hernquist, L., et al. 2017, *MNRAS*, 465, 3291

Weingartner, J. C. & Draine, B. T. 2001, *ApJ*, 548, 1, 296

Wells, M., Pel, J.-W., Glasse, A., et al. 2015, *PASP*, 127, 646

Whitcomb, C. M., Smith, J.-D. T., Sandstrom, K., et al. 2024, *ApJ*, 974, 1, 20

Whitcomb, C. M., Smith, J.-D. T., Tarantino, E., et al. 2025, *ApJ* submitted, arXiv:2509.18347

Wright, G. S., Rieke, G. H., Glasse, A., et al. 2023, *PASP*, 135, 1046, 048003

Xie, Y. & Ho, L. C. 2022, *ApJ*, 925, 218

Yuan, F. & Narayan, R. 2014, *ARA&A*, 52, 529

Zhang, L. & Ho, L. C. 2023, *ApJL*, 953, L9

Zhang, L., Ho, L. C., & Li, A. 2022, *ApJ*, 939, 22

Zhang, L., García-Bernete, I., Packham, C., et al. 2024b, *ApJL*, 975, 1, L2

Zhang, L., Packham, C., Hicks, E. K. S., et al. 2024a, *ApJ*, 974, 2, 195

Zhang, L., Davies, R. I., Packham, C., et al. 2025, *ApJS* 280, 65

## APPENDIX

## A. PAH DECOMPOSITION

Figures A1, A2, and A3 for PAH decompositions of NGC 1266, NGC 3190, and NGC 4736.

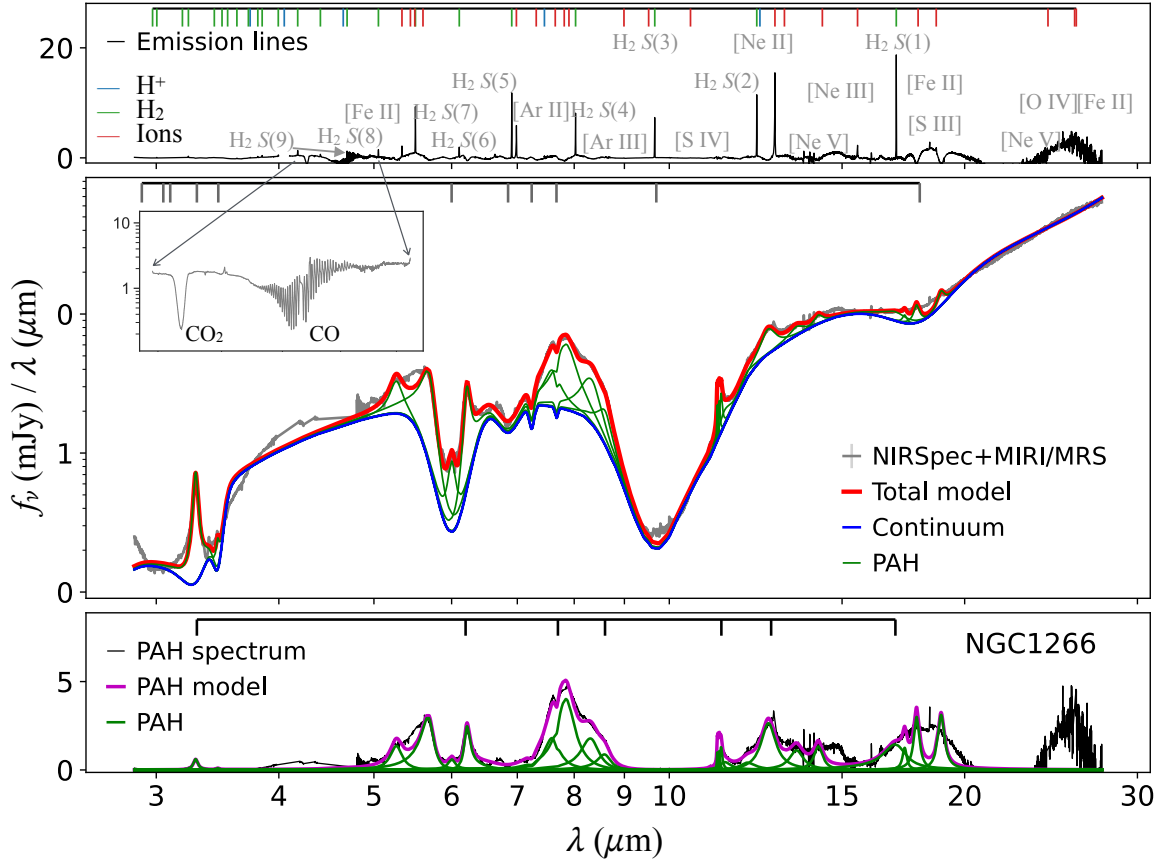


**Figure A1.** The same as Figure 1 but for NGC 1266.

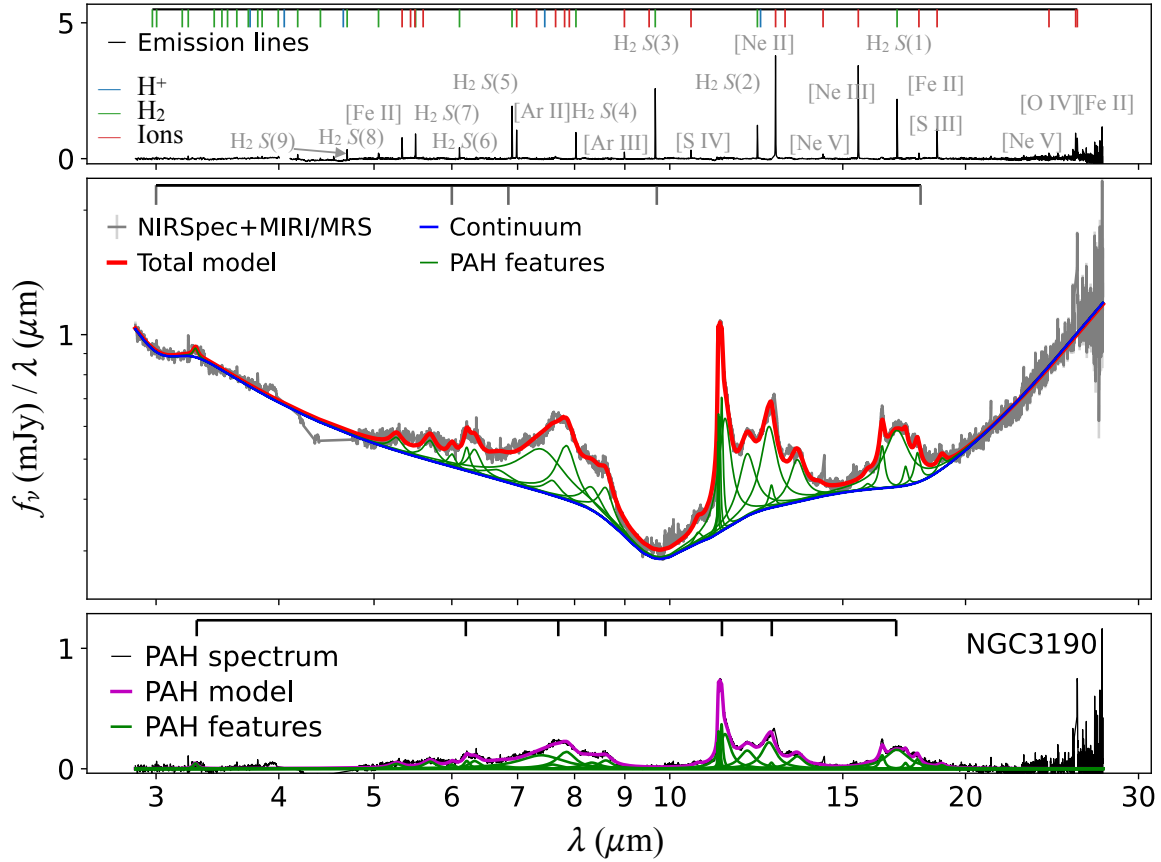


**Figure A2.** The same as Figure 1 but for NGC 3190.

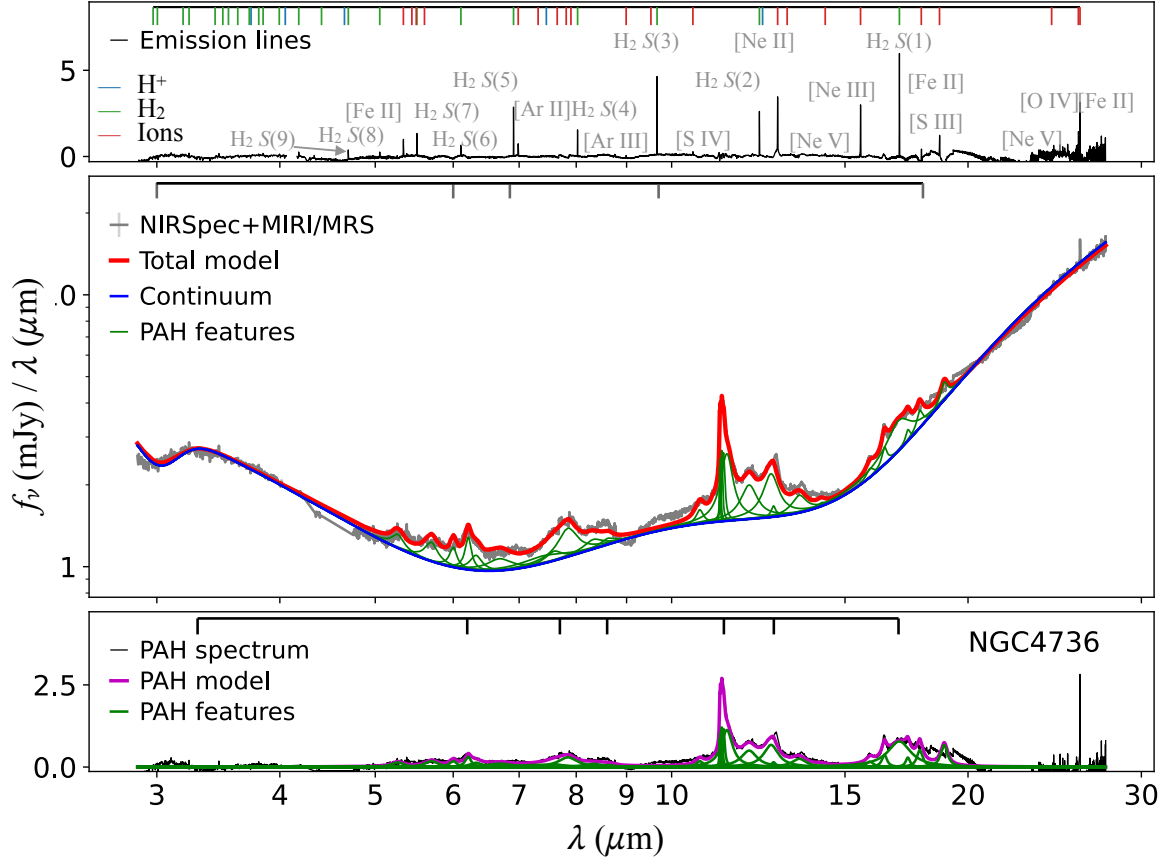


**Figure A3.** The same as Figure 1 but for NGC 4736.

B. H<sub>2</sub> POPULATION DIAGRAMS

The flux of an H<sub>2</sub> transition at energy level  $J$ ,  $F(J)$ , is related to the H<sub>2</sub> column density in the upper level,  $N(J_{\text{up}})$ , by  $F(J) \propto A \times N(J_{\text{up}})/\lambda$ , where  $A$  and  $\lambda$  are the Einstein coefficient and wavelength of the corresponding H<sub>2</sub> transition, respectively.

Assuming local thermal thermodynamic (LTE) and a realistic power-law distribution of the H<sub>2</sub> level populations as a function of temperature  $T$ , i.e.,  $dN = mT^{-\beta}dT$ , with  $m = N_{\text{tot}}(\beta - 1)/(T_l^{1-\beta} - T_u^{1-\beta})$ , the column density of each H<sub>2</sub> pure rotational transition can be expressed as  $N(J) = m \int_{T_l}^{T_u} \frac{g(J)}{Z(T)} e^{-E(J)/kT} T^{-\beta} dT$  (Togi & Smith 2016; see also Hunt et al. 2025). This relation is fitted to the observed relative populations of the H<sub>2</sub> pure rotational transitions to derive the free parameters (see the left panels of Figure A4). Following Togi & Smith (2016), we fit for the lower-end temperature ( $T_l$ ) and the power-law index ( $\beta$ ), while fixing the upper-end temperature at  $T_u = 3500$  K. The adopted  $T_u$  is higher than that used by Togi & Smith (2016) ( $T_u = 2000$  K), since the fitting here includes H<sub>2</sub> pure rotational transitions from H<sub>2</sub> S(1) through H<sub>2</sub> S(16), whereas Togi & Smith (2016) considered transitions from H<sub>2</sub> S(0) through H<sub>2</sub> S(7). The best-fit values of  $T_l$  and  $\beta$ , together with the corresponding total H<sub>2</sub> column density ( $N(H_2)$ ) under LTE, are shown in the upper right corners of the left panels in Figure A4.

The LTE assumption does not hold here when the fitting includes both H<sub>2</sub> pure rotational and ro-vibrational transitions, although the power-law distribution of H<sub>2</sub> level populations as a function of temperature remains applicable. In this case, the column density of each H<sub>2</sub> pure rotational or ro-vibrationa transition can be expressed as  $N(J) = m \int_{T_l}^{T_u} n(T, n(H_2), n(H)) T^{-\beta} dT$  (Pereira-Santaella et al. 2014), where  $m$  is defined as above, and  $n(T, n(H_2), n(H))$  represents the fractional H<sub>2</sub> population at level  $J$  at given temperature for an environment with H<sub>2</sub> and H number densities of  $n(H_2)$  and  $n(H)$ , respectively. This relation is fitted to the observed relative populations of the H<sub>2</sub> pure rotational and ro-vibrational transitions using  $n(T, n(H_2), n(H))$  numerically calculated by Pereira-Santaella et al. (2014) (available with  $J$  up to 14) to derive the free parameters (see the right panels of Figure A4). Following Pereira-Santaella et al. (2014), we fit for  $\beta$ ,  $n(H_2)$  and  $n(H)$ , while fixing the lower- and upper-end temperatures at  $T_l = 200$  K and  $T_u = 3500$  K. The best-fit values of  $\beta$ ,  $n(H_2)$  and  $n(H)$ , together with the corresponding total H<sub>2</sub> column density ( $N(H_2)$ ) under non-LTE conditions, are shown in the upper right corners of the right panels in Figure A4.

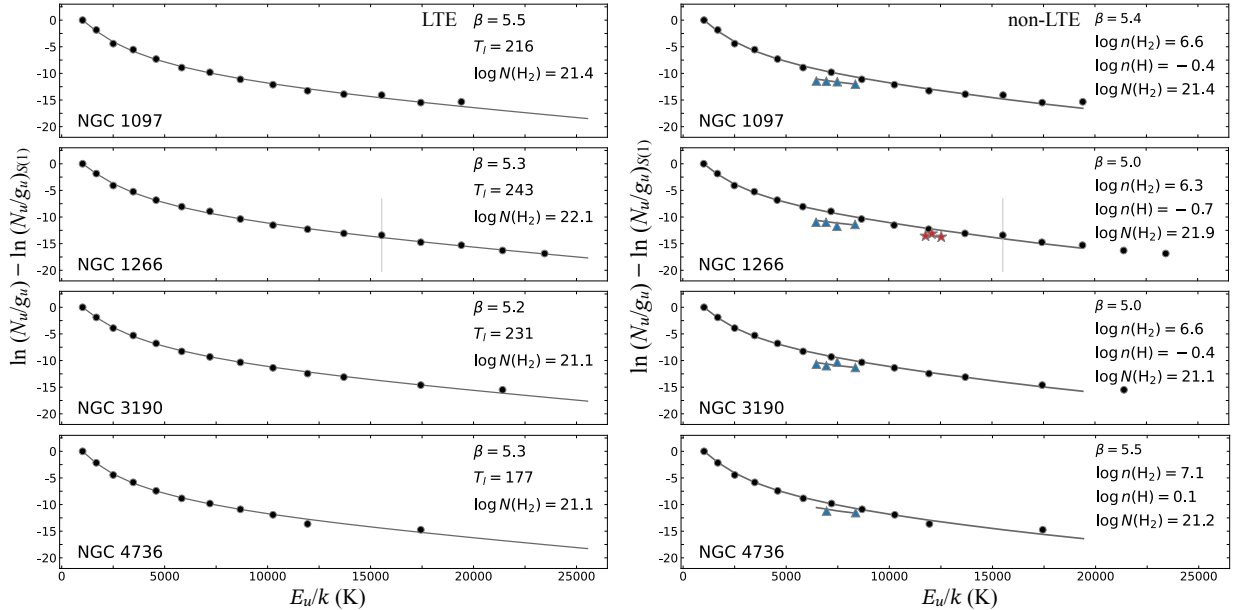


**Figure A4.** H<sub>2</sub> population diagrams of (left) the pure rotational transitions and (right) the pure rotational and ro-vibrational transitions. Black dots in each panel represent the relative populations of the H<sub>2</sub> pure rotational transitions, H<sub>2</sub> S(1) through H<sub>2</sub> S(16), arranged from left to right if detected. Blue triangles in right panels represent the relative populations of the H<sub>2</sub> ro-vibrational transitions, H<sub>2</sub> 1-0 O(4) through H<sub>2</sub> 1-0 O(7), arranged from left to right if detected. Red stars in the right panel of NGC 1266 represent the relative populations of the H<sub>2</sub> ro-vibrational transitions, H<sub>2</sub> 2-1 O(3), H<sub>2</sub> 2-1 O(4), and H<sub>2</sub> 2-1 O(5), arranged from left to right. The black curves show the predicted population distributions based on the best-fit parameters labeled in the top right of each panel, assuming LTE for the H<sub>2</sub> pure rotational transitions in the left panels and non-LTE conditions for the H<sub>2</sub> pure rotational and ro-vibrational transitions in the right panels, as detailed in Section B. Note that the H<sub>2</sub> column density ( $N(H_2)$ ) labeled in each panel is derived assuming an equivalent aperture size of  $1'' \times 1''$  for each nuclear region.

## C. ABSORPTION AND EMISSION MEASUREMENTS

Tables for measurements of silicate and ice absorptions (Table A1), PAH features (Table A2), ionized emission lines (Table A3), and H<sub>2</sub> transitions (Table A4) involved in this work.

**Table A1.** Measurements of Silicate and Ice Absorptions

Component	FWHM	$\log \tau^{\text{NGC 1097}}$	$\log \tau^{\text{NGC 1266}}$	$\log \tau^{\text{NGC 3190}}$	$\log \tau^{\text{NGC 4736}}$
(-)	( $\mu\text{m}$ )	(-)	(-)	(-)	(-)
(1)	(2)	(3)	(4)	(5)	(6)
Silicate <sup>†</sup>	...	-4.98	0.45	-0.58	-5.01
Ice <sub>3.0 \mu\text{m}</sub> <sup>‡</sup>	0.353	-1.43	...	-0.88	-0.48
-2.90 $\mu\text{m}$	0.101	...	-4.97	...	...
-3.05 $\mu\text{m}$	0.294	...	-0.44	...	...
-3.10 $\mu\text{m}$	0.212	...	-1.31	...	...
-3.30 $\mu\text{m}$	0.294	...	0.09	...	...
Ice <sub>3.47 \mu\text{m}</sub>	0.094	...	-0.09	...	...
Ice <sub>6.0 \mu\text{m}</sub>	0.577	-1.83	0.32	-4.99	-5.02
Ice <sub>6.85 \mu\text{m}</sub>	0.398	-1.97	-0.31	-4.99	-5.00
Ice <sub>7.24 \mu\text{m}</sub>	0.099	...	-0.42	...	...
Ice <sub>7.674 \mu\text{m}</sub>	0.066	...	-0.76	...	...

NOTE—Optical depths of silicate and ice absorptions. [†]: The infrared extinction curve of Smith et al. (2007) is given by the optical depth  $\tau(\lambda)$  normalized by the peak value at 9.7  $\mu\text{m}$ ,  $\tau(9.7\mu\text{m})$ , as listed in the first row. [‡]: The extinction of each ice absorption component is given by the optical depth  $\tau(\lambda)$  modeled with a Gaussian profile using a fixed FWHM and a fitted amplitude as listed.

**Table A2.** Measurements of PAH Features

PAH features	$\log f_{\text{PAH}}^{\text{NGC 1097}}$	$\log f_{\text{PAH}}^{\text{NGC 1266}}$	$\log f_{\text{PAH}}^{\text{NGC 3190}}$	$\log f_{\text{PAH}}^{\text{NGC 4736}}$
(-)	[erg/s/cm <sup>2</sup> ]	[erg/s/cm <sup>2</sup> ]	[erg/s/cm <sup>2</sup> ]	[erg/s/cm <sup>2</sup> ]
(1)	(2)	(3)	(4)	(5)
PAH <sub>3.3 \mu\text{m}</sub>	-14.09 $\pm$ 0.09	-12.10 $\pm$ 0.08	-14.46 $\pm$ 0.10	...
PAH <sub>6.2 \mu\text{m}</sub>	-13.30 $\pm$ 0.05	-11.82 $\pm$ 0.08	-13.77 $\pm$ 0.07	-13.34 $\pm$ 0.07
PAH <sub>7.7 \mu\text{m}</sub>	-12.79 $\pm$ 0.05	-11.62 $\pm$ 0.06	-12.94 $\pm$ 0.06	-12.90 $\pm$ 0.06
PAH <sub>11.3 \mu\text{m}</sub>	-12.89 $\pm$ 0.06	-12.26 $\pm$ 0.04	-13.12 $\pm$ 0.06	-12.61 $\pm$ 0.07

NOTE—Flux measurements of PAH features.

**Table A3.** Measurements of Ionized Emission Lines

Ionized lines	$\lambda$	IP	$\log f_{\text{NGC 1097}}$	$\log f_{\text{NGC 1266}}$	$\log f_{\text{NGC 3190}}$	$\log f_{\text{NGC 4736}}$
(-)	( $\mu\text{m}$ )	(eV)	[erg/s/cm $^2$ ]	[erg/s/cm $^2$ ]	[erg/s/cm $^2$ ]	[erg/s/cm $^2$ ]
(1)	(2)	(3)	(4)	(5)	(6)	(7)
[Fe II]	5.34	7.9	$-14.60 \pm 0.06$	$-14.06 \pm 0.02$	$-14.64 \pm 0.00$	$-14.63 \pm 0.03$
[Ar II]	6.985	15.8	$-14.24 \pm 0.03$	$-13.53 \pm 0.01$	$-14.50 \pm 0.02$	$-14.74 \pm 0.01$
[Ar III]	8.991	27.6	$-14.99 \pm 0.02$	$-15.08 \pm 0.07$	$-15.14 \pm 0.15$	$-15.45 \pm 0.10$
[S IV]	10.511	34.8	$-14.84 \pm 0.07$	$-15.50 \pm 0.13$	$-15.06 \pm 0.02$	$-15.37 \pm 0.09$
[Ne II]	12.814	21.6	$-13.70 \pm 0.04$	$-13.10 \pm 0.01$	$-13.89 \pm 0.03$	$-13.96 \pm 0.01$
[Ne V]	14.322	97.1	$-15.41 \pm 0.05$	$< -15.79$	$-15.42 \pm 0.01$	$-15.63 \pm 0.02$
[Ne III]	15.555	41.0	$-13.97 \pm 0.03$	$-13.82 \pm 0.03$	$-13.94 \pm 0.02$	$-14.11 \pm 0.04$
[S III]	18.71	23.3	$-14.37 \pm 0.11$	$-14.12 \pm 0.21$	$-14.36 \pm 0.10$	$-14.45 \pm 0.08$
[O IV]	25.89	54.9	$-14.39 \pm 0.16$	$< -14.83$	$-14.65 \pm 0.20$	$-14.54 \pm 0.28$

NOTE—Flux measurements of ionized emission lines.

**Table A4.** Measurements of H<sub>2</sub> Transitions

H <sub>2</sub> transitions	$\lambda$	$\log f_{\text{NGC 1097}}$	$\log f_{\text{NGC 1266}}$	$\log f_{\text{NGC 3190}}$	$\log f_{\text{NGC 4736}}$
(-)	( $\mu\text{m}$ )	[erg/s/cm $^2$ ]	[erg/s/cm $^2$ ]	[erg/s/cm $^2$ ]	[erg/s/cm $^2$ ]
(1)	(2)	(3)	(4)	(5)	(6)
H <sub>2</sub> S(1)	17.035	$-13.80 \pm 0.01$	$-13.23 \pm 0.02$	$-14.12 \pm 0.01$	$-13.97 \pm 0.01$
H <sub>2</sub> S(2)	12.279	$-14.06 \pm 0.01$	$-13.50 \pm 0.02$	$-14.41 \pm 0.01$	$-14.37 \pm 0.01$
H <sub>2</sub> S(3)	9.665	$-13.96 \pm 0.01$	$-13.26 \pm 0.02$	$-14.07 \pm 0.01$	$-14.14 \pm 0.01$
H <sub>2</sub> S(4)	8.025	$-14.35 \pm 0.01$	$-13.65 \pm 0.02$	$-14.56 \pm 0.01$	$-14.64 \pm 0.01$
H <sub>2</sub> S(5)	6.91	$-14.16 \pm 0.01$	$-13.39 \pm 0.03$	$-14.26 \pm 0.01$	$-14.38 \pm 0.01$
H <sub>2</sub> S(6)	6.109	$-14.94 \pm 0.01$	$-14.00 \pm 0.03$	$-14.99 \pm 0.01$	$-15.07 \pm 0.01$
H <sub>2</sub> S(7)	5.511	$-14.51 \pm 0.01$	$-13.57 \pm 0.03$	$-14.63 \pm 0.01$	$-14.68 \pm 0.01$
H <sub>2</sub> S(8)	5.053	$-15.27 \pm 0.02$	$-14.38 \pm 0.02$	$-15.26 \pm 0.01$	$-15.34 \pm 0.02$
H <sub>2</sub> S(9)	4.6947	$-14.98 \pm 0.02$	$-14.15 \pm 0.05$	$-14.98 \pm 0.01$	$-15.06 \pm 0.01$
H <sub>2</sub> S(10)	4.4096	$-15.73 \pm 0.04$	$-14.74 \pm 0.05$	$-15.70 \pm 0.04$	$-16.06 \pm 0.11$
H <sub>2</sub> S(11)	4.181	$-15.34 \pm 0.02$	$-14.41 \pm 0.02$	$-15.32 \pm 0.01$	...
H <sub>2</sub> S(12)	3.9947	$-15.72 \pm 0.21$	$-14.87 \pm 3.00$	$-14.90 \pm 0.07$	...
H <sub>2</sub> S(13)	3.8464	$-15.70 \pm 0.03$	$-14.81 \pm 0.03$	$-15.65 \pm 0.02$	$-15.54 \pm 0.07$
H <sub>2</sub> S(14)	3.724	$-15.98 \pm 0.05$	$-15.40 \pm 0.04$	...	...
H <sub>2</sub> S(15)	3.625	...	$-15.23 \pm 0.03$	$-15.78 \pm 0.05$	...
H <sub>2</sub> S(16)	3.547	...	$-15.86 \pm 0.05$	...	...
H <sub>2</sub> 1-0 O(4)	3.0039	$-15.85 \pm 0.06$	$-15.09 \pm 0.01$	$-15.85 \pm 0.06$	...
H <sub>2</sub> 1-0 O(5)	3.235	$-15.43 \pm 0.03$	$-14.65 \pm 0.02$	$-15.53 \pm 0.02$	$-15.48 \pm 0.05$
H <sub>2</sub> 1-0 O(6)	3.5007	$-16.01 \pm 0.07$	$-15.51 \pm 0.04$	$-15.78 \pm 0.05$	...
H <sub>2</sub> 1-0 O(7)	3.8075	$-15.83 \pm 0.03$	$-14.99 \pm 0.02$	$-15.84 \pm 0.03$	$-15.78 \pm 0.03$

**Table A4** *continued*

**Table A4** (*continued*)

H2 transitions	$\lambda$	$\log f_{\text{NGC 1097}}$	$\log f_{\text{NGC 1266}}$	$\log f_{\text{NGC 3190}}$	$\log f_{\text{NGC 4736}}$
(-)	( $\mu\text{m}$ )	[erg/s/cm $^2$ ]	[erg/s/cm $^2$ ]	[erg/s/cm $^2$ ]	[erg/s/cm $^2$ ]
(1)	(2)	(3)	(4)	(5)	(6)
H <sub>2</sub> 2-1 <i>O</i> (3)	2.9741	...	$-15.61 \pm 0.03$	...	...
H <sub>2</sub> 2-1 <i>O</i> (4)	3.1899	...	$-15.87 \pm 0.05$	...	...
H <sub>2</sub> 2-1 <i>O</i> (5)	3.4379	...	$-15.68 \pm 0.03$	...	...

NOTE—Flux measurements of H<sub>2</sub> transitions.